JGR Solid Earth

RESEARCH ARTICLE
10.1029/2025JB032002

Observations of Small-Scale Heterogeneity in the Upper Mantle Beneath Old Oceanic Lithosphere

A. Hariharan[1,2], Z. Eilon[1], J. Gaherty[3], J. Russell[4], J. Phillips[3], and D. Forsyth[5]

[1]Department of Earth Science, University of California Santa Barbara, Santa Barbara, CA, USA, [2]Institute of Geophysics and Planetary Physics, Scripps Institution of Oceanography, UC San Diego, La Jolla, CA, USA, [3]School of Earth and Sustainability, Northern Arizona University, Flagstaff, AZ, USA, [4]Department of Earth and Environmental Sciences, Syracuse University, Syracuse, NY, USA, [5]Department of Earth, Environmental, and Planetary Sciences, Brown University, Providence, RI, USA

Key Points:

- High-resolution body-wave imaging of the upper mantle below old oceanic lithosphere in a region characterized by free-air gravity lineations
- Substantial heterogeneity in the asthenospheric mantle implies thermal anomalies and potentially melt
- These results add to growing observational evidence of top-driven small-scale convection beneath oceanic lithosphere

Supporting Information:

Supporting Information may be found in the online version of this article.

Correspondence to:

A. Hariharan,
anhariharan@ucsd.edu

Citation:

Hariharan, A., Eilon, Z., Gaherty, J., Russell, J., Phillips, J., & Forsyth, D. (2025). Observations of small-scale heterogeneity in the upper mantle beneath old oceanic lithosphere. *Journal of Geophysical Research: Solid Earth*, *130*, e2025JB032002. https://doi.org/10.1029/2025JB032002

Received 18 MAY 2025
Accepted 4 DEC 2025

Author Contributions:

Conceptualization: Z. Eilon, J. Gaherty, D. Forsyth
Data curation: A. Hariharan
Formal analysis: A. Hariharan
Funding acquisition: Z. Eilon, J. Gaherty, D. Forsyth
Investigation: A. Hariharan
Methodology: A. Hariharan, Z. Eilon, J. Gaherty, J. Russell, D. Forsyth
Project administration: Z. Eilon, J. Gaherty, D. Forsyth
Resources: Z. Eilon
Software: A. Hariharan, Z. Eilon
Supervision: Z. Eilon
Validation: A. Hariharan
Visualization: A. Hariharan
Writing – original draft: A. Hariharan

Abstract We present tomographic images of the velocity structure of the upper mantle beneath old (~90 Ma) oceanic lithosphere, derived from arrival time measurements of teleseismic body waves recorded by ocean-bottom seismometers. Differential travel time measurements on *P*, *S*, and *SKS* body waves across a wide range of frequency bands show consistent geographic and backazimuthal variations that highlight substantial velocity heterogeneity in the upper mantle beneath the array. A joint inversion of all data sets shows that the information in the *P* and *S* times are consistent with each other. The amplitude of apparent velocity heterogeneity and the scaling between independently constructed δV_p and δV_s tomographic models is consistent with either the presence of melt and ~50°K thermal anomalies or, if melt free, <100°K thermal anomalies. δV_p and δV_s tomographic models both show statistically meaningful elongation of structure along an approximately NW-SE axis, subparallel to the orientation of free-air gravity lineations and absolute plate motion. We interpret the overall structure as evidence for convective processes associated with the delamination of old lithosphere. Our work adds to a growing body of observational evidence that highlights strong heterogeneity in the oceanic upper mantle, potentially suggesting widespread small-scale convection.

Plain Language Summary At several locations in the oceans, parallel, and alternating linear features can be observed in measurements of gravitational acceleration. Understanding the origin of such features enables us to better understand the evolution of tectonic plates. To study the Earth's interior at one of these locations, we acquired data from an array of seismometers placed there. Using measurements of the times at which seismic waves from distant earthquakes were observed at these seismometers, we developed three-dimensional images of how fast seismic waves travel. We found significant variations in the speeds shown in these images, which also show oriented features roughly parallel to the gravity anomalies. These images provide evidence for rising and sinking material in the Earth's interior at this location. This evidence, along with previous work, supports a hypothesis whereby this convective process may be common, particularly beneath mature oceanic plates.

1. Introduction

The seafloor subsides with increasing age due to conductive loss of heat to the surface and the accompanying thermal contraction of the lithosphere. Although a purely conductive model, that is, a half-space cooling model (e.g., Parker & Oldenburg, 1973), can provide a good approximation of the average subsidence and heat flow for the first 70–80 Ma of seafloor evolution, it has long been recognized that there must be some non-conductive source of heat to the base of the lithosphere that slows subsidence of older seafloor. A phenomenological thermal model that satisfies average global subsidence and heat flow for all ages is a plate cooling model with a fixed lithospheric thickness and a fixed basal temperature (e.g., Sleep, 1969; Sclater & Francheteau, 1970). However, the simplicity of the plate cooling model obscures the necessary complexity of some process in the asthenosphere that supplies additional heat to maintain a constant temperature at depth. Two basic forms of convection have been suggested as candidates for this process: upwelling of hot plume material from depth (e.g., Crough, 1978); and small-scale convection that removes or delaminates the lower part of the cooling lithosphere, replacing it with hotter asthenosphere (Parsons & McKenzie, 1978; Richter & Parsons, 1975).

Undoubtedly, both forms of convection are important. For example, the estimates of thermal plate thickness depend on which topographic data are included; Parsons and Sclater (1977) estimated a thickness of about 125 km

Writing – review & editing:
A. Hariharan, Z. Eilon, J. Gaherty, J. Russell, J. Phillips, D. Forsyth

for the North Pacific plate, avoiding obvious seamount provinces and hotspots, while Stein and Stein (1992) estimated values of only about 95 km, based on including all the topographic data. Pronounced spatial differences in subsidence rate across mid-ocean ridges (Cochran, 1986) may also be an indication of sub-lithospheric flow in the mantle from hotspots (Conder et al., 2002; Toomey et al., 2002). Korenaga and Korenaga (2008) argues that essentially all of the older Pacific lithosphere has been modified by flow from hotspots forming seamount provinces and broad hotspot swells.

One of the most prominent arguments for the role of small-scale convection is the existence of lineated, oscillatory, free-air anomalies oriented obliquely to fossil spreading directions and approximately parallel to the absolute motion direction of the plate (Cazenave et al., 1992; Haxby & Weissel, 1986). Shear in the asthenosphere between the plate and the underling deeper mantle tends to organize small-scale convection into linear rolls (commonly called "Richter rolls") oriented in the direction of shear (Richter & Parsons, 1975). However, free-air gravity or geoid anomalies provide very little information about the nature of the convection. An upwelling, low-density line of anomalous mantle induces convective motion that tends to deflect the surface upwards (e.g., Buck & Parmentier, 1986; Parsons & Daly, 1983). However, inherent tradeoffs in joint investigations of bathymetric and gravimetric data make it challenging to accurately resolve the characteristics of such anomalous mantle (Harmon et al., 2007; Richards & Hager, 1989). Information from seismic images of the upper mantle provides a complementary perspective on the nature of convective heterogeneity.

The purpose of the OldORCA (this study) and YoungORCA experiments (Eilon, Gaherty, et al., 2022) was to conduct seismological studies of the upper mantle beneath two areas of Pacific seafloor that display quasi-linear alternating free-air gravity anomalies. Very few prior experiments have had sufficient bathymetric and seismological coverage to shed light on the origin of the gravity lineaments. The Gravity Lineations Intraplate Melting Petrologic and Seismic Expedition project (GLIMPSE) covered very young seafloor (<10 Ma) west of the East Pacific Rise (Forsyth et al., 2006). In that area, there are narrow volcanic ridges within free-air anomaly lows oriented in the spreading direction perpendicular to the spreading center, which led to models of their origin such as lithospheric boudinage (Sandwell et al., 1995) and cracking of the plate by thermal contraction (Sandwell & Fialko, 2004). However, it turns out that the free air anomaly (FAA) minima are due to flanking flexural lows created by the loading of the volcanic ridges; when the full response is accounted for, the ridges actually lie on top of a broader swell, analogous to the Hawaiian swell (Harmon et al., 2006). The swell region is underlain by low-velocity mantle, indicating that the origin of the gravity lineaments and volcanic ridges is most likely banded flow in the asthenosphere toward the ridge from the Pacific superswell region, perhaps also triggering local small-scale convection (Harmon et al., 2011; Holmes et al., 2007), but the vertical resolution available for body (Harmon et al., 2007) and surface wave (Weeraratne et al., 2007) tomography in GLIMPSE was insufficient to resolve much more than the sign of the velocity anomalies in the lithosphere and shallow asthenosphere.

The YoungORCA region lies on seafloor that is about 40 Ma old (Figure 1a). Unlike the GLIMPSE area, the gravity lineaments are oriented obliquely to neighboring fracture zones and there are no prominent volcanic ridges. However, the bathymetric coverage is limited, so accounting for topographic effects is imperfect. Full analysis of the data from YoungORCA is incomplete, but body wave tomography shows that there are significant (up to ±2%) *P*-wave velocity anomalies in the upper mantle, quasi-parallel to the gravity lineaments and extending to depths of at least 250 km (Eilon, Zhang, et al., 2022), pointing to the importance of small-scale convection.

The OldORCA region lies in the Cretaceous quiet zone with no identifiable magnetic anomalies, so its spreading history is somewhat unclear, with the reconstructions from Seton et al. (2020) and Eagles et al. (2004) disagreeing on the precise age. The reconstruction from Eagles et al. (2004) suggests an age of approx. 90 Ma beneath the array, with isochrons that are approximately parallel to seafloor abyssal-hill fabric; a nominal age estimate of approximately 85–95 Ma is consistent with spreading from the Phoenix ridge at a constant rate. The existence of short-wavelength gravity lineaments associated with old seafloor is unusual and worthy of investigation. Fortunately, the area was thoroughly mapped previously in a search for subtle magnetic anomalies (Gee et al., 2008), so there is excellent bathymetric coverage. Seismic studies are needed to determine whether there is any remaining structure in the shallow mantle associated with the volcanic ridges or evidence of deeper, sub-lithospheric convection as found beneath YoungORCA (Eilon, Zhang, et al., 2022).

To provide constraints on mantle structure at a resolution sufficient to infer regional mantle dynamics, we apply body-wave tomography. Images of seismic wavespeeds derived from differential body-wave travel times

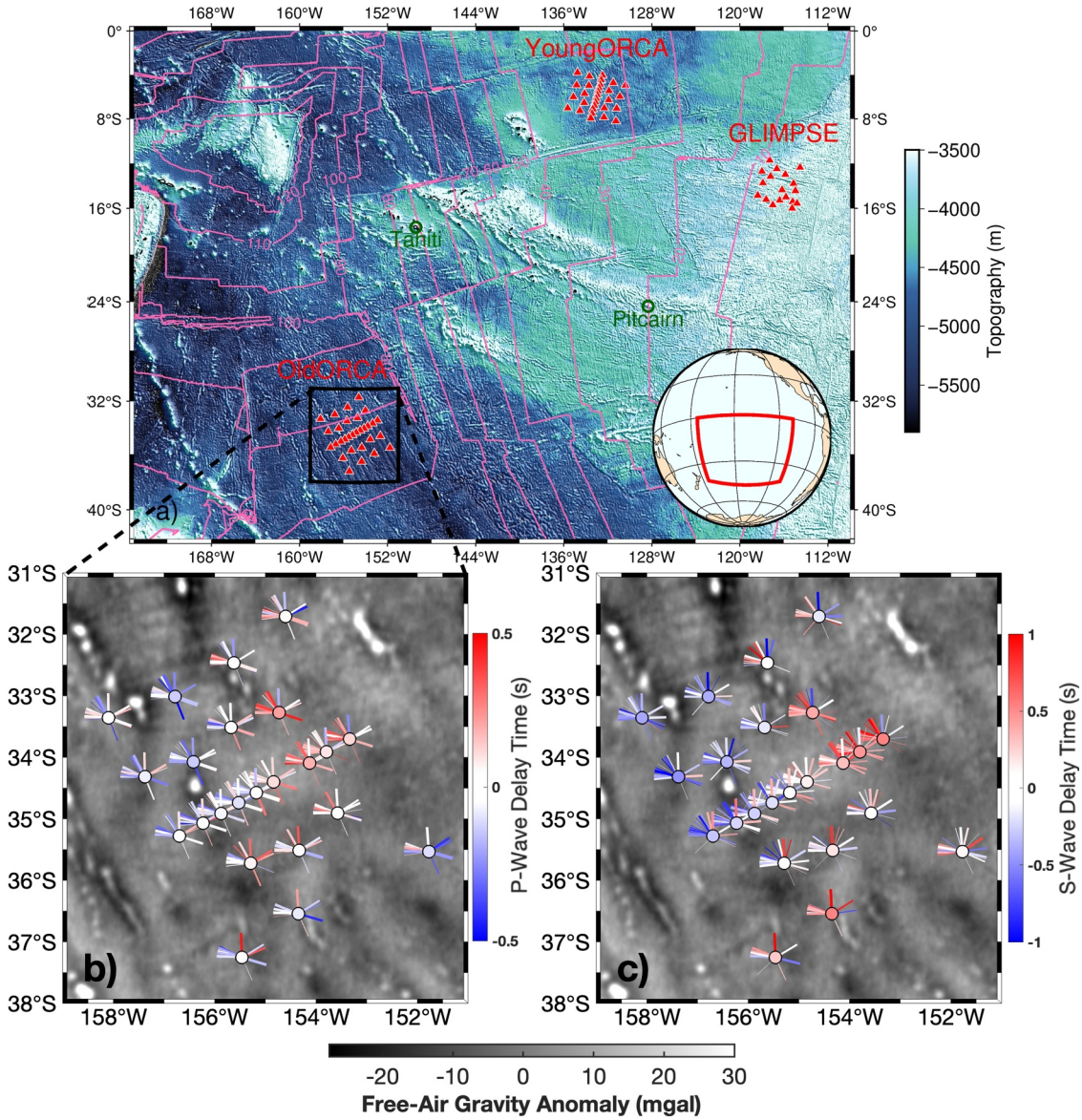

Figure 1. (a) Regional map, showing bathymetry from the SRTM+ model (Tozer et al., 2019). Overlain is a merged model of seafloor age, using the study of Eagles et al. (2004) within the OldORCA region and the study of Seton et al. (2020) elsewhere (Phillips et al., 2023). Arrays of broadband seismometers overlying gravity lineations (the OldORCA, YoungORCA, and GLIMPSE arrays) are shown as red triangles. The red polygon in the inset world map corresponds to the bounding edges of panel (a). Zoomed-in panels show (b) *P*-wave and (c) *S*-wave relative delay times plotted as spokes at each station, with the orientation of each spoke corresponding to measurement backazimuth and colored according to the amplitude of the delay time. For measurements that were made at multiple frequencies, the values are averaged across all frequencies (only for ease of visualization in this figure). The width of a spoke is proportional to the number of frequencies that go into a single measurement. Refer to the supporting information (Figures S8 and S9 in Supporting Information S1) for separate visualization of raw measurements at each frequency, which show very similar patterns to those shown here. The background color in (b) and (c) is the free-air gravity anomaly (Sandwell et al., 2014).

generally have higher lateral resolution of the oceanic upper mantle than constraints from fundamental-mode surface waves, and image deeper structure, well into the asthenosphere. Previous body-wave imaging studies targeting the mantle beneath oceanic lithosphere have observed substantial velocity heterogeneity. Harmon et al. (2007) observed relative delay times that are not consistent with a homogeneous asthenosphere; they inferred active processes such as small-scale convection. At YoungORCA, the amplitude of inferred velocity heterogeneity was consistent with as much as ∼300° − 500°K lateral temperature variations (Eilon, Zhang, et al., 2022). Beneath very old (160–180 Ma) oceanic lithosphere, Kang et al. (2023) applied multi-frequency finite-frequency body wave tomography and tomographically imaged even more substantial *P*-wave velocity variations of ±4%, consistent with substantial temperature variations that likely exceed the solidus and necessitate

the presence of melt. In this study, we present teleseismic *P* and *S* models of the upper mantle at the OldORCA location, adding to this growing body of local and high-resolution studies of the oceanic upper mantle.

2. Data and Methods

2.1. The Measurement of Differential Arrival Times

The OldORCA array of OBS stations (Eilon, Gaherty, et al., 2022) is composed of 30 broadband Trillium T-240 three-component seismometers (Figure S1 in Supporting Information S1), with differential pressure gauges (DPGs), operated by the Scripps Institution of Oceanography. The array has an average station separation of ∼80 km, with a maximum aperture of ∼630 km. Stations were deployed for ∼13 months, between November 2019–2020. Of the 30 instruments deployed, 23 returned good seismic data on all three components, enabling high-quality body-wave delay time measurements (Figures S1 and S2 in Supporting Information S1).

We use a catalog of earthquakes with magnitudes between 5.5 and 7.8 at epicentral degrees between 30 and 95° for *P*-waves, 30 and 84° for *S*-waves, and 86 and 132° for *SKS*-waves. For these events, we download waveforms, rotate individual stations using the orientation corrections published in Eilon, Gaherty, et al. (2022), and remove the instrument response to velocity. After decimating the waveforms to a 10 Hz sample rate, we make measurements of pairwise phase lags between different stations for different events using multichannel cross-correlation (VanDecar & Crosson, 1990) on *P*-waves separately observed on the vertical component and DPG, *S*-waves on the transverse component and *SKS*-waves on the radial component. This well-established method uses a least-squares approach to solve for the best-fitting map of relative travel times that is consistent with phase lags measured at all pairs of stations across the array.

Prior to obtaining time lags from cross-correlation, we manually inspect and window waveforms, striving to isolate just the "first break" of the body wave waveform while also including a significant amount of pre-signal noise to stabilize the cross-correlation calculation and ensure that the peak in the correlogram corresponds to the body wave that is targeted (Figure S2 in Supporting Information S1). The width of the time segment used to window the waveform approximately scales with the longest period in the period band under consideration. Delay time measurements are made on waveforms that are filtered across a range of frequency bands using two-pole Butterworth filters, where the edges of the period bands were chosen to avoid overlap with noise associated with the spectral peak corresponding to the secondary microseism (Janiszewski et al., 2023). We use differential traveltimes measured at period bands of 12–50, 9–45, 8–40, 8–30, 8–25, 7–20, 2–5, 1–5, 2–4, 1.66–3.33, 1–2, and 0.5–2.5 s. We account for overlapping information in these frequency bands by using a weighting scheme that ensures that the overlap in frequency content between measurements does not lead to the repeated use of redundant, or non-independent measurements, and this weighting scheme is described in more detail in the following section. In Section 3.3 and Text S3 in Supporting Information S1, we present calculations that show that our use of multi-frequency measurements does not bias the interpretable structure.

2.2. The Tomographic Inversion

We follow a standard approach for teleseismic finite-frequency body-wave tomography, using a specific implementation developed by Schmandt and Humphreys (2010), and subsequently built upon by Eilon et al. (2015) and Brunsvik et al. (2021). For the inversion, we minimize a cost function, *E*, that penalizes data misfit, model norm, and model roughness as follows:

$$E = \|\mathbf{W}(\mathbf{Gm} - \mathbf{d})\|^2 + \gamma\|\nabla^2\mathbf{m}_v\|^2 + \epsilon\|\mathbf{m}_v\|^2 + \epsilon_{evt}\|\mathbf{c}_e\|^2 + \epsilon_{sta}\|\mathbf{c}_s\|^2 \quad (1)$$

In this formalism, **G** is a matrix consisting of kernels that describe the sensitivity of a given datum to the model parameters, **m** is a model vector consisting of slowness perturbations ($\mathbf{m}_v$) to the starting 1-D model, concatenated with station static terms $\mathbf{c}_s$, and event terms $\mathbf{c}_e$. Station static terms account for local bathymetric/sediment/crustal structure that affect all arrivals at a given station. Event terms account for the (common) case where only a subset of stations records an event, shifting the average delay for those arrivals (arbitrarily fixed to zero in the cross-correlation step) to be consistent with the whole array. **d** is the data vector of relative delay times. ϵ_i control the strength of model parameter damping, and γ controls the strength of second-derivative smoothing. We assign the ratio of vertical to horizontal smoothing as 0.5. 10 × additional damping is implemented at shallowest and deepest layers of model nodes to avoid edge effects.

The finite-frequency kernels (populating rows of **G**) are calculated following the approach of Schmandt and Humphreys (2010) and Brunsvik et al. (2021), and represent a first-fresnel zone approximation to the full "banana-donut" kernels (Marquering et al., 1999). Since these kernels vary as the center period at which a measurement is made changes, this enables us to incorporate measurements at the same source-receiver combination, but at different frequencies (see Section 2.1), into our inversion. The impact of considering the frequency-dependent sensitivity of traveltimes is clearest when considering the lateral width, or "fatness" of the kernel for any given measurement, since this width increases with the square root of the central period of the wave (Hung et al., 2000). Incorporating the varying frequency-dependent sensitivity of traveltimes is therefore generally considered to improve resolution and sharpen the amplitudes of the resultant images, relative to a purely ray-theoretical implementation (Affonso et al., 2021; Hung et al., 2004; Montelli et al., 2004).

Each measurement is assigned a weight in the tomographic inversion with weighting matrix **W**. The weighting accounts for (a) a metric of measurement uncertainty calculated using Equation 8 in VanDecar and Crosson (1990), which quantifies the extent to which individual measurements of lag time are fit by the single-station time at the relevant station (this weight dominates the composite weighting; Figure S6 in Supporting Information S1), (b) waveform similarity (between stations, not frequencies) as quantified by correlation coefficient with the stack, (c) the waveforms' SNR, and (d) our multi-frequency scheme, which weights measurements based on how much independent information each frequency provides relative to complementary measurements at other frequencies that share the same source-station path. The latter term allows us to include multi-frequency measurements without overly emphasizing signals from earthquakes that provide more "broadband" constraints in terms of viable measurement frequencies (Figure S3 in Supporting Information S1). Text S1 in Supporting Information S1 describes our weighting in more detail. Through this weighting scheme, measurements are up-weighted as they span both a more unique range of the frequency domain, and a wider range in the frequency domain, thus ensuring that the value of the independent information that a measurement provides is emphasized. Due to the long tail of the distribution of the VanDecar and Crosson (1990) uncertainty estimates, which dominate the composite weights (Figure S4 in Supporting Information S1), the resulting weights can be large, and so weights are capped at a value of 4× the mean weight. We find that the weights from the approach of VanDecar and Crosson (1990) correlate well with weights based on the correlation coefficients (Figure S5 in Supporting Information S1), suggesting that the individual components of the weights are accurately and consistently capturing the inherent robustness of the measurements.

We independently solve for compressional and shear wavespeed models, defined as fractional slowness perturbations to a 1-D model (s_0), so $\mathbf{m}_v = (\mathbf{s} - s_0)/s_0$. For ease of interpretation, we convert these values to fractional velocity perturbations, discussed henceforth. The models are parameterized on a cartesian grid oriented northwards (tests show that the orientation of the grid has a negligible impact on the inversions), with 30 km horizontal spacing at the center, scaling to 80 km spacing at twice the array aperture, and 35 km vertical spacing. The model space is defined between 40 and 500 km depth. We use the iasp91 model (Kennett & Engdahl, 1991) to trace raypaths, the same model used to predict phase move-out for relative delay times. The inverse problem is solved using the LSQR algorithm (Paige & Saunders, 1982), running for a maximum of 5,000 iterations with a convergence criterion characterized by an error tolerance of $1e-5$, and data fit is quantified in terms of the (weighted) variance reduction (e.g., Schmandt & Humphreys, 2010; Eilon et al., 2015). To explore the compatibility of P and $*S$ data sets, we also perform a joint inversion of all travel times for a joint δV_S model, where we impose an assumed scaling for slowness perturbations: $\delta v_p = R\delta v_s$. We set $R = 0.55$, as is consistent with heterogeneity primarily governed by thermal variations (Karato, 1993).

3. Results

In this section, we first describe features of the raw differential travel time measurements, and then present results from our joint and independent tomographic inversions.

3.1. Delay Times

Our final data set of measurements are obtained using conservative quality control metrics (eliminating measurements with an SNR below 3.5 and a correlation coefficient with the stack of aligned waveforms that falls below 0.8). In general, we find that the highest-quality measurements correspond to events with larger magnitudes ($\approx \geq 6$) and periods above the secondary microseism peak. For P-waves, we also obtain some high-quality

measurements at periods below the secondary microseism peak. This joint control that both period band and earthquake magnitude exert on measurement characteristics can be seen through a visualization of SNR as a function of frequency and magnitude for all earthquakes recorded by our stations (Figure S6 in Supporting Information S1). This highlights, for all phases, a decline in measurement SNR as the frequency corresponding to the secondary microseism is approached, and for *P*-waves, a subtle increase in measurement SNR as frequencies increase past the secondary microseism. The measurements have good backazimuthal coverage (Figure S7 in Supporting Information S1), though with a preponderance of events from the west, along the Sunda subduction zone.

Our final data set contains 1987 *S* and *SKS* delay times and 1847 *P* delay times, making this a uniquely comprehensive data set relative to some other recent body wave studies; Kang et al. (2023) and (Eilon, Zhang et al., 2022) did not present *S*-wave observations, and we recorded a larger number of measurements than the study of Harmon et al. (2007), though the multifrequency nature of our data set entails some redundancy. We observe consistent back-azimuthal and geographic variations, as well as patterns that persist across frequency bands and across both *P* and *S* measured phases. Moreover, the values of the corresponding relative delay times of *P* and *S* show a covariance that highlights the agreement between the independently measured *P*- and *S*-wave data sets (Figure 1).

The distributions of arrival times span a large range and follow an approximately Gaussian distribution. For *P*-waves, the central 80% of the travel time distribution falls between −0.30 and +0.32 s; the overall RMS is 0.25 s. For *S*-waves, the corresponding spread is −0.69 to +0.71 s, with an RMS of 0.56 s. The larger range (by approximately a factor of 2.25) for *S*-waves is consistent with the ratio of ∼1.9 − 2.2 estimated for the temperature dependence of upper mantle materials with no melt present, based on laboratory measurements (Forsyth, 1992; Ritzwoller et al., 1988).

Since *P*- and *S*- patterns are so similar, we first describe the systematics they share, before highlighting some modest differences. Delay times at northeast stations from northwesterly azimuths are significantly delayed relative to the average. At the same northeast stations, arrivals from the NNE are early relative to the average. At stations in the west, arrivals are overall fast, particularly for arrivals from the NW. The dense line of stations along the spine of the array shows a clear transition in delay times, from generally faster in the west to more delayed in the east. At stations in the south, arrivals from the north and northwest are delayed relative to the average. However, measurements corresponding to azimuths from the east are somewhat sped up relative to the average. Although some stations are overall slower and others overall faster, the unambiguous backazimuthal variations, repeated with great similarity across several individual stations, imply strong lateral velocity gradients are present in the mantle beneath the study area.

For both *P*- and *S*-waves, the patterns described above are generally consistent across all the frequency bands explored (Figures S8 and S9 in Supporting Information S1), with only minor differences. For example, for S waves, some of the most advanced (faster) relative arrivals are recorded at the west-most stations, along azimuths consistently from the northwest. While the P waves also record fast delay times for these source-station paths, they are not unambiguously the fastest in the study area along these paths. We also note that the southwest-most station consistently shows delayed arrivals from the northwest at all frequencies for S-waves, but not for P-waves. As a sanity check, we find that *P*-wave measurements made on the DPG show similar patterns as for the vertical components (Figure S9 in Supporting Information S1); however, as there are a small number of high-quality measurements from the DPGs, we do not incorporate these in the inversions, and all *P* measurements used in the inversion are from the vertical component. From an orthogonal regression of the independent *P* and *S* delay times with weights proportional to the calculated variances, we find a clear correlation between P/S delay time with a slope consistent with thermally governed heterogeneity that highlights the expected scaling between these independent observations (Figure S10 in Supporting Information S1), but the actual value of this slope is too poorly constrained to be interpreted in terms of the underlying physical mechanism.

3.2. Tomographic Model

In this study, we present independent V_p and V_s tomographic models for our study region, as well as a jointly inverted, scaled V_p and V_s model derived from both *P* and *S* data sets. Figure 2 shows horizontal slices of our preferred models, and Figure 3 shows vertical cross-sections through these models. In this section, we first present

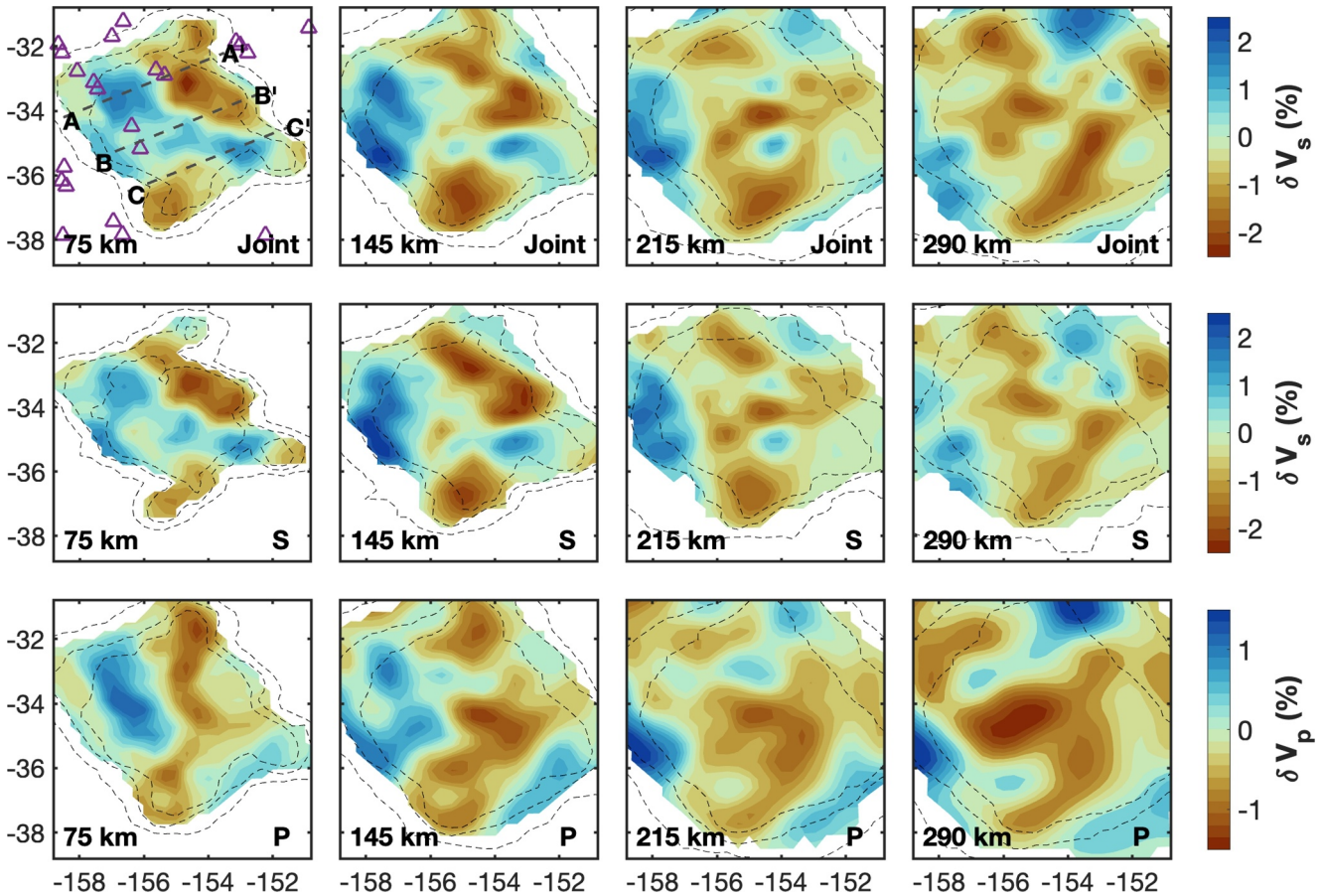

Figure 2. Summary of preferred joint δV_s (top row), individual δV_s (middle), and δV_p (bottom) models at a range of depths. The overlaid dashed lines corresponds to 0.6, 0.4, and 0.2 contours of hit quality; regions with hit quality less than 0.3 are masked out. Each column corresponds to a different depth, which is shown in the bottom-left corner. Purple triangles in the top-left panel correspond to local seamounts from the compilation of Kim and Wessel (2011).

an exploration of the model space (for both joint and individual inversions) that arises from variable choices of regularization. We then discuss the features of our preferred joint and independent tomographic models in detail.

3.2.1. A Suite of Models

Regularization parameters (smoothing (γ) and damping (ϵ) values) are somewhat subjective, but exert significant control on tomographic models. A common heuristic to obtain preferred regularization is to pick a model that corresponds to a point located at the elbow of an "L-curve" that describes the classic trade-off between data fit and model simplicity (Figure 4, Figure S11 in Supporting Information S1). Since we recognize that this choice is subjective and that no unique regularization parameters are "correct," our philosophy for exploring and understanding the velocity heterogeneity implied by our analysis for this study is to present (and analyze) a suite of models spanning the entire viable region of the L-curve space (Figures S12–S23 in Supporting Information S1), allowing the reader to better appreciate which features of the model are robust. We discuss this decision, as well as alternate approaches for arriving at a preferred model, in more detail in Text S2 in Supporting Information S1, and highlight some key factors that impede an alternative approach here.

A choice of preferred model couched in maximum likelihood theory would ideally yield a reduced-χ^2 estimate (Text S2 in Supporting Information S1) near unity for both P and S-wave models, suggesting levels of data fit similar to estimates of measurement error, where such estimates are derived from the approach of VanDecar and Crosson (1990). However, our analyses yielded reduced-χ^2 values for the majority of the model suite that were generally much higher than unity (for *S* models) and less than unity (for *P* models) (Figure S24 in Supporting Information S1). We found that choosing a preferred model using these reduced-χ^2 values would necessitate

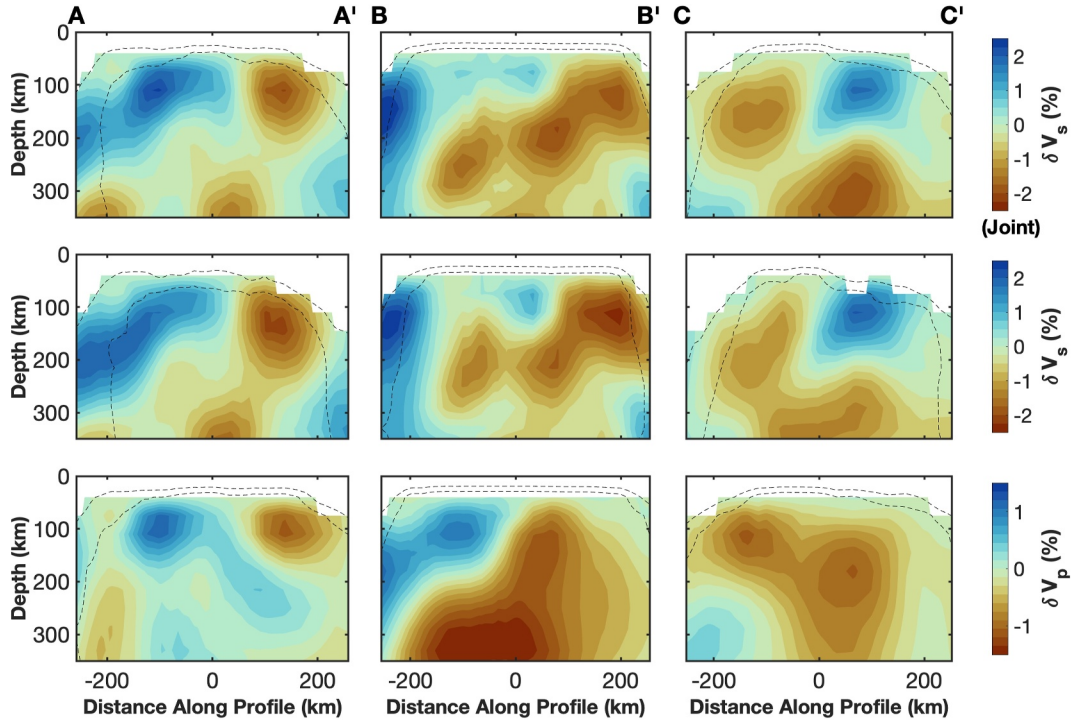

Figure 3. Vertical cross-sections through our δV_p (top), δV_s (middle), and joint inversion (bottom) models, corresponding to the transects that are shown in Figure 2. Overlain are dashed hit quality contours of 0.4 and 0.6.

significantly increasing the regularization in the *P*-wave models and decreasing the regularization in the *S*-wave models, yielding inconsistent structure between models and unexpectedly high-amplitude $\delta V_s/\delta V_p$ structure; such an approach thus seemed inadvisable for our inversion. The underlying differences between the reduced-χ^2 values for *P* and *S*-wave models are driven by the much larger RMS amplitude of the *S*-wave traveltimes relative to the *P*-wave traveltimes (the former being larger by approximately a factor of 2) while in the presence of estimated data errors with relatively similar amplitudes (Figure S7 in Supporting Information S1). We interpret this as implying that our formal estimates of data error may be incomplete. Rigorous explorations of teleseismic *P* and *S*-wave delay time uncertainties have not been conducted on OBS data, and we identify this as an area for future exploration and beyond the scope of this study. For now, we thus rely on a rigorous analysis of the model space and a presentation of the full model suite as heuristics to assess the reliability of the inverted models.

In all our inversions, the amplitude and wavelength of heterogeneity varies predictably as we explore different damping and smoothing parameters (Figure 4 and Figure S11 in Supporting Information S1); increased smoothing (γ) leads to smoother and longer-wavelength structure and increasing damping (ϵ) reduces the amplitudes of the models. Figures S12–S14 in Supporting Information S1 show the results of the joint inversion for a range of choices of damping and smoothing parameters. To summarize the consistency of model features across these different choices of regularization, we map regions of consistently fast and consistently slow structure via depth-dependent vote maps, which depict how consistent a particular model characteristic is across a suite of models (Lekic et al., 2012; Ritsema & Lekić, 2020). We calculate separate vote maps for both high and low velocities, as follows: For each model corresponding to combinations of damping/smoothing sampled evenly between 0 and 20, we add a "vote" at any voxel with velocity perturbation exceeding a low or high-velocity threshold (±0.75% for *S* waves, and ±0.4% for *P* waves). Figure 5 presents these vote maps for the suite of models generated from the joint inversion. At shallow depths, the vote maps highlight consistently slow structure in the north and south of the model, with the zone of slow structure in the north showing elongation NW-SE. Similarly, at shallow depths, we see a zone of high-velocity structure in the west of the model, but also showing a NW-SE elongation. At deeper depths, the center of the model is characterized by slower structure of significant amplitude; the shallow high-velocity lineament pattern begins to distort slightly at depths below 145 km, and

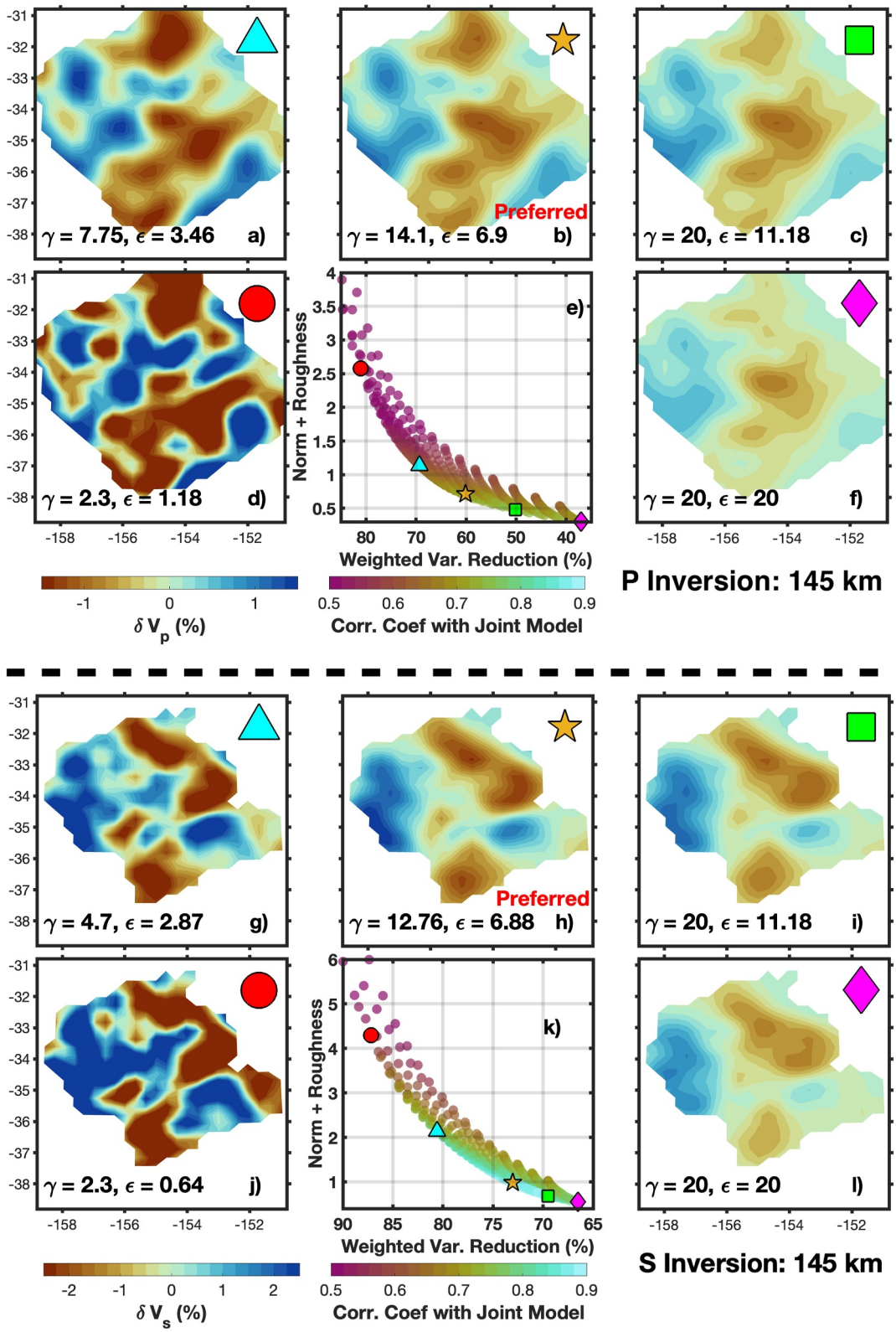

Figure 4.

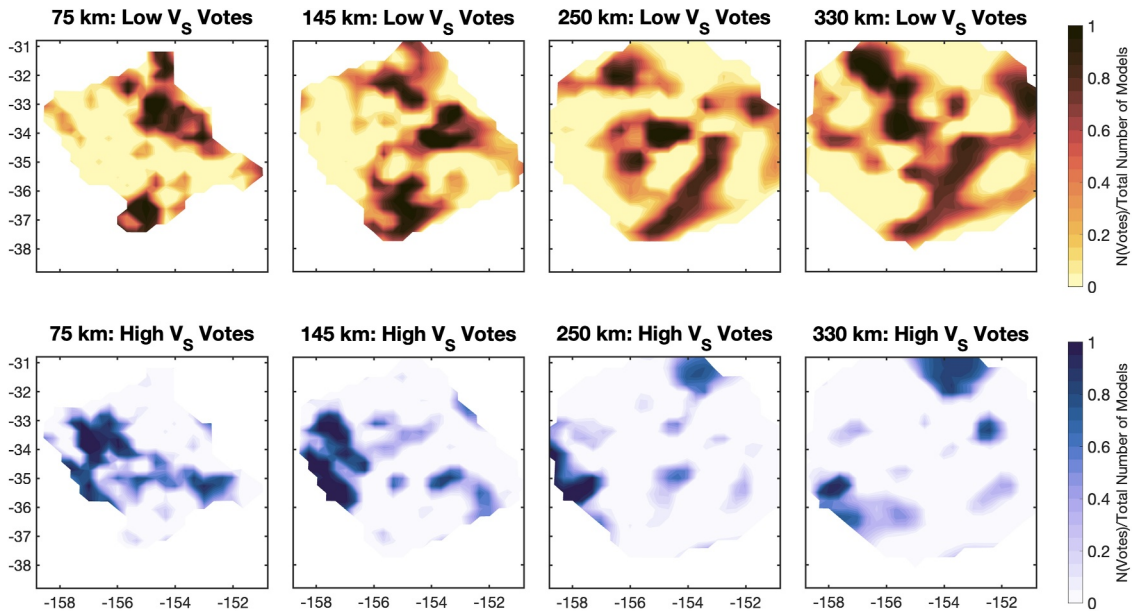

Figure 5. Vote maps documenting the consensus on high and low-velocity structure that is implied by results from the joint inversion. The vote maps summarize results from joint inversions conducted using a wide range of damping and smoothing parameters, between 0 and 20. The number of votes at any pixel are normalized by the total number of models that were queried (400). The threshold velocity required for a successful 'vote' is ±0.75%. The Supporting Information S1 contains similar figures for the independent *P* and *S* inversions.

reorganizes into a more complex, less linear structure. At the deeper depths in the model, we image a NW-SE zone of low velocities.

By visualizing the individual results from independent inversions for a range of choices of regularization (Figures S15–S20 in Supporting Information S1) and summarizing consistent structure in vote maps in Figure S21 and S22 in Supporting Information S1 for *S* and *P* waves respectively, we observe consistent structure across a wide suite of models derived from the independent *P* and *S* data sets. The majority of the realizations of *P* and *S* models show a NW-SE oriented high-velocity streak at the shallowest depths in the south of the model (Figure S21 and S22 in Supporting Information S1). At the same shallow depths, there is a low-velocity feature in the north of the models. In *S*-wave models this feature is sub-parallel to the high-velocity streak, but for the *P*-wave models it is more arcuate. In the south, all models again agree on low velocities, but the *S* models imply more clear separation between this slow feature and the northern one. At intermediate depths (≈145km), *S*-wave models continue to show a pair of NW-SE-oriented high and low-velocity lineations, but these are much less clear for the *P*-wave models. An apparent reorganization of structure is more evident in both models at deeper depths; the *S*-wave models tend to show a NW-SE lineation of low velocities at deeper depths (particularly evident in the vote map, Figure S21 in Supporting Information S1), but the *P*-wave models, while also manifesting low velocities in the center of the model, do not show clear lineation. In a later section, we rigorously explore the extent to which the models prefer oriented structure. We also find (Figure S23 in Supporting Information S1) that as damping and smoothing increases, simplifying the models to only the coarsest features required by the data, the (independent) δV_s and δV_p models show an increasing correlation with each other. This result shows that there are consistent underlying patterns in the structure seen by both *P* and *S* data sets.

Figure 4. Illustration of (at a depth of 145 km) how models from the inversion for the independent δV_p and δV_s models vary as a function of damping and smoothing, and selection of the preferred model: showing examples of a relatively underdamped model (triangle), our preferred model (star), a relatively smooth model (square), a model that is both under-damped and very under-smoothed (circle), and (diamond) a model that is over-damped and over-smoothed. Panels (e) and (k) show the L-curves for the *S* and *P*-models respectively, illustrating the choice of the preferred model and the placement of the other illustrative models on the L-curve. The corresponding smoothing and damping parameters (γ, ϵ) corresponding to each model are shown. The colorscale on the L-curves provides the correlation coefficient between each individual model and the preferred joint model.

3.2.2. Preferred Model Features

Our preferred joint model, which falls on the elbow of the corresponding L-curve (Figure S11 in Supporting Information S1), shows the features we described in the vote map of the full model suite, while not showing the spurious structure that is visible for lower values of damping and smoothing. We select preferred regularization for the independent models from a combination of proximity to the "elbow" of the L-curve and a high correlation with the model from the joint inversion, which is shown via color shading of the L-curves for the independent models (Figure 4). The preferred independent *S*-wave model tends to show better correlation with the model from the joint inversion than the *P*-wave model, likely because the *S*-wave data has larger amplitudes (Figure 1), though this may also be consistent with the higher sensitivity of shear moduli to melt and temperature. The models achieve a reasonable fit to the data, and show a weighted variance reduction of 73% for the *S*-wave data set and 60.1% for the *P*-wave data set. In a later section, we demonstrate that these variance reductions are significant.

Our preferred models are shown in map view in Figure 2 and cross-section in Figure 3. In general, structure is consistent across the joint, independent *P*, and independent *S* models. At shallow depths ($\leq$150 km), our preferred joint and *S*-wave models have relatively low-velocity structure in the northeast and southwest of the model. However, the center of the model is characterized by a lineament of high velocity structure, trending NW-SE and most prominent at shallow depths in the model. At deeper depths (215 km), the center of the model begins to be characterized by slower structure of significant amplitude; the shallow high-velocity lineament pattern distorts at depths below 110 km, and reorganizes between 145 and 215 km into a more complex, less linear structure. At even deeper depths ($z \geq 290$ km) we once again see a NW-SE lineament, slightly displaced horizontally from the shallow lineament, but this time demarcating low velocities rather than high velocities and spanning a larger lateral width. Our *P*-wave model shows similar patterns at shallower depths and also exhibits a reorganization of velocity patterns at middle depths, but in this *P*-wave model, the low-velocity feature at deeper depths is perhaps oriented more E-W as opposed to NW-SE. All models also show some structure oriented ENE-WSW; at $\sim 110-145$ km, there is a low-velocity lineament oriented ENE-WSW. This structure is approximately sub-parallel to and co-located with the first-order variation in bathymetry across the array, which takes the form of a sharp decrease over a very small distance from ~ -5000 m to ~ -5400 m (Figure S1), which is also co-located with the location at which gravity lineations are somewhat disrupted.

In cross-section view, we see narrow and alternating high and low-velocity regions in the upper region of the model, with a relatively low-velocity zone at deeper depths of large amplitude that is displaced laterally from shallower low-velocity regions. The alternating shallow high and low velocity zones are clearest along cross-sections A-A′ and B-B′; section C-C′ falls along a location where we see subtle low-velocity lineament oriented ENE-WSW for the *P*-wave models. All three transects highlight the similarity between the (independent) *P*-wave and *S*-wave models, though cross-section C-C′ lacks shallow high-velocity structure while still having all three models be consistent on the other locations of low-velocity structure.

The station terms solved for in our inversion show relatively small amplitudes ($\sim$0.04 s for *P* waves and $\sim$0.02 s for *S* waves). The patterns in station terms are somewhat similar for both *P* and *S* waves (Figure S24 in Supporting Information S1) and show geographic coherence, suggesting that they are accounting for real structure. The low amplitude of the station terms is consistent with relatively homogeneous sediment properties and crustal thickness across the study region, (the latter of which is suggested by trends in global compilations of crustal thickness observations (Van Avendonk et al., 2017)), at least in the context of teleseismic body wave travel times.

3.3. Evaluating Model Robustness

In this section, we summarize the results of several tests that we have conducted to assess and understand the robustness of our preferred model. More details about these tests are provided in Text S3 in Supporting Information S1.

First, we address the significance of the moderate variance reduction that we observe (73% for the *S*-wave model, 60% for the *P*-wave model). To demonstrate that our models' variance reduction is significant, we test a null hypothesis—that the data are *only* random noise, and that the inversion is simply fitting this noise with meaningless structure. We generated and subsequently inverted synthetic data sets characterized by only random noise (Text S3 in Supporting Information S1). For both the *P* ($V_R \approx 16.7\%$) and *S*-wave data sets ($V_R \approx 19.9\%$), the variance reduction is significantly lower (30-sigma for *S*-waves, and 25-sigma for *P*-waves) than the variance

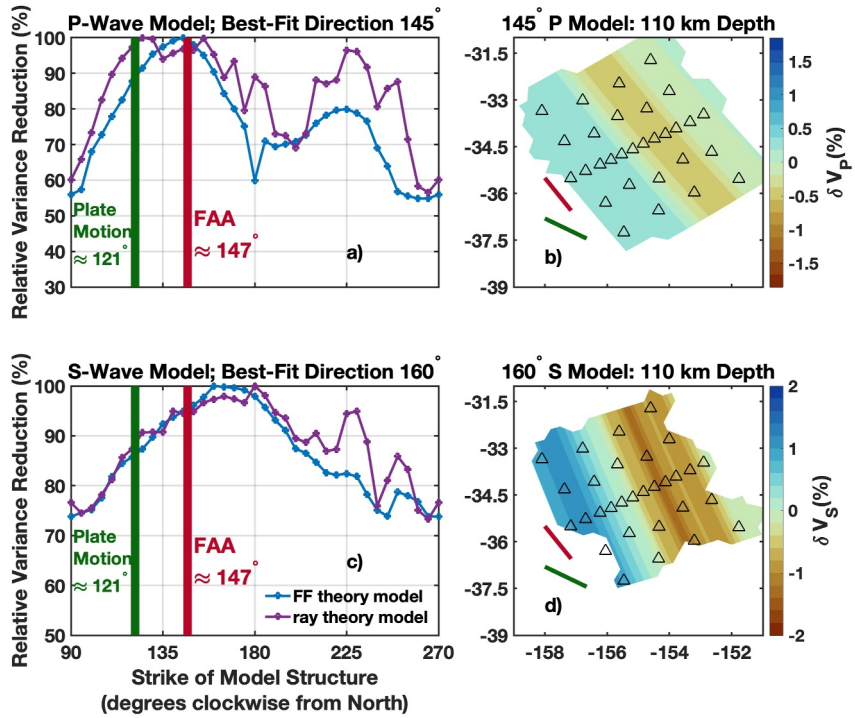

Figure 6. Results of a test to explore the extent to which heterogeneity at a constant orientation can adequately explain our data. (a, c): Variance reduction (Relative to global maximum) as a function of the orientation of model structure, for (a) the *P*-wave data set and (c) the *S*-wave data set. Also shown (b, d) are the inverted models that correspond to the best-fitting strike for both the *P*- and *S*-wave inversions. Shown as colored lines in panel (d) are the orientations of the free-air gravity anomaly lineations for our study regions and the orientation of absolute plate motion in a no-net rotation reference frame for the ITRF2020 model (Altamimi et al., 2023). Note the consistency between the best-fitting orientation for both *P*- and *S*-wave data sets, as well as the consistency in the locations of the low and high-velocity anomalies for the *P*- and *S*-wave inverted models.

reductions obtained from inverting real data (Figure S25 in Supporting Information S1). This suggests that our inversions represent good fits to noisy data, and that our models are meaningful.

As an additional test of model robustness, we perform tomographic inversions on our real data, but this time using a ray-theoretical approach instead of using finite-frequency (FF) kernels. We found that, for both joint and independent P and S models, the ray-theoretical inversion results (Figures S26 and S27 in Supporting Information S1) showed patterns that are broadly consistent with those in the finite-frequency models, attesting to the robustness of these patterns.

Synthetic tests help evaluate the spatial resolution of our inversions and identify biases in imaged structure. "Checkerboard" tests, which test the recovery of input structure organized in a checkerboard pattern, show good recovery overall, with recovery best at the center of the model and with some deterioration and smearing toward the southwest in the western section of the model and toward the northeast in the eastern section of the model (Figure 7, Text S3 and Figure S28 in Supporting Information S1). We also perform synthetic tests to evaluate the recovery of oriented structure, since such structure is an important aspect of our model interpretation. We observe excellent recovery of input structure organized in orientations both parallel and perpendicular to the gravity lineations (Figures S30 and S31 in Supporting Information S1), with no distortion of the orientation of the structure, suggesting that the observed lineations are not an artifact of ray geometry for our limited earthquake catalog.

To explore whether the data support interpreting the apparent NW-SE lineation, we perform a "2.5D" test where we force the model to be uniform along a single azimuth (i.e., varying only in depth and the orthogonal direction) (Eilon, Zhang, et al., 2022). We vary this azimuth to determine whether the data imply structural lineation, and how large this preference is (Figure 6). For this test we use finite-frequency kernels and the preferred model

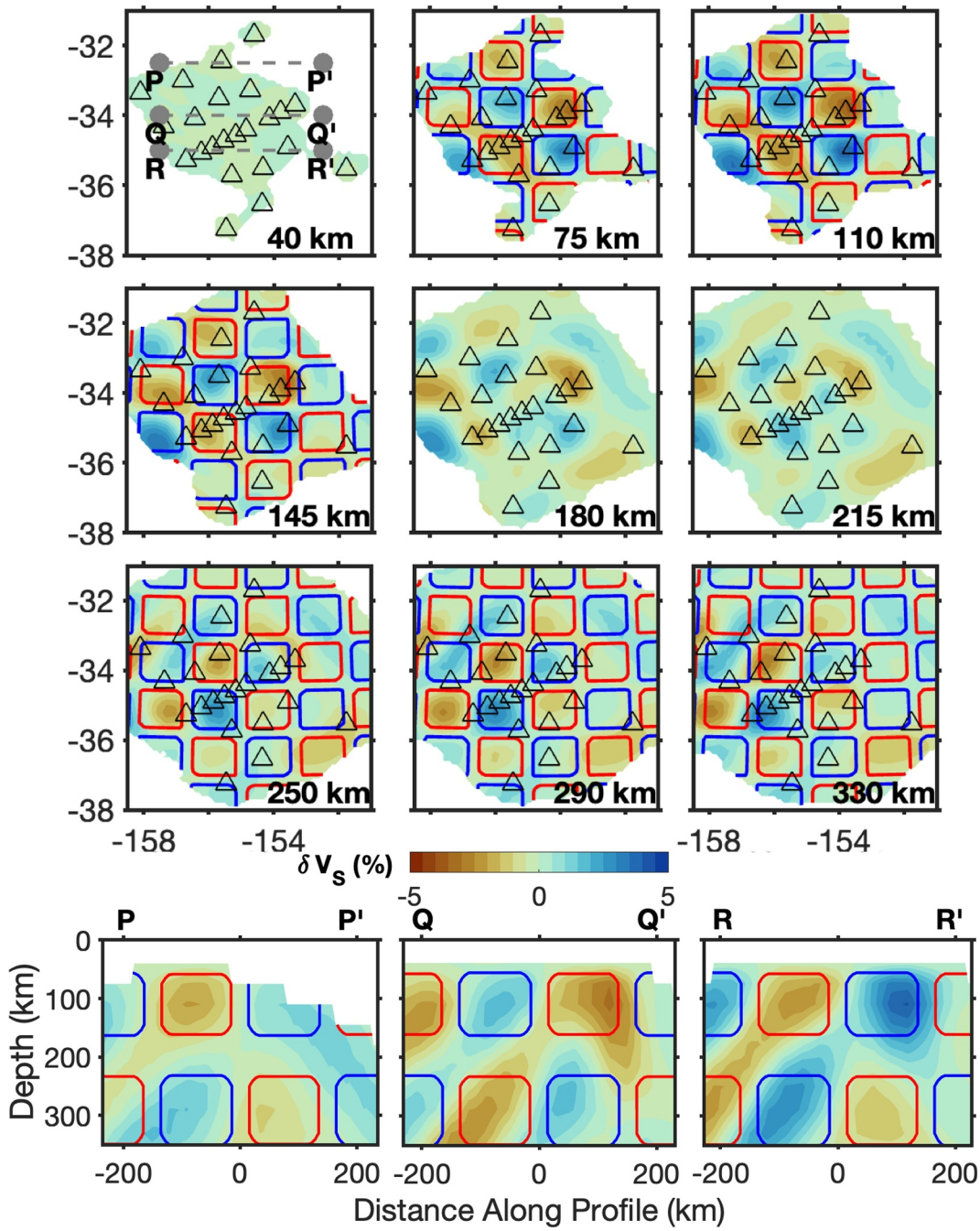

Figure 7. Results of *S*-wave checkerboard tests. Top three rows; horizontal slices showing the recovery of checkerboard tests at different depths. Bottom row: E-W sections through the output model, with corresponding transects shown in the top-left panel. Only sections of the model with hit quality ≥0.4 are shown. The locations and shapes of input low and high-velocity checkers of amplitude ±5% are shown with red and blue contours respectively.

regularization parameters. We find that, consistent with the visual appearance of oriented heterogeneity in our preferred model, the best-fit orientation is ∼145° for the *P*-wave model, and ∼160° for the *S*-wave model. In this context, the optimal "2.5D" model has a variance reduction of ∼58%, which is significantly better than the worst-fit 2.5D model (42%).

Next, we explore the extent to which depth-dependent variations in heterogeneity are necessary in our preferred model. If we allow no variation in structure as a function of depth, we observe a significant decrease in variance

reduction (49% for the *S*-wave model), suggesting that depth-dependent structure is important to explain some of the data. To explore this further, we "squeeze" model structure by confining the model to a limited range of depths (Figures S32 and S33 in Supporting Information S1) and examine the patterns and data fit of the resulting models (Text S3 in Supporting Information S1). We find that while the data do prefer some variation with depth, it is much less important than the first-order lateral variations, which are very consistent across varying squeezing depths; however, the precise depth of the significant anomalies in our model is quite poorly constrained.

We also execute tests to confirm that our inversion is not unduly impacted by the presence of redundant or non-independent multifrequency data. We conduct an inversion where we only invert the subset of measurements that are from non-overlapping frequency bands for each earthquake (Text S3; Figures S34, S35 in Supporting Information S1), and find that the features of the resulting model are consistent with our preferred model. We also explore the impact of our choice of data weighting by conducting a suite of multiple inversions where the data weights are randomized (Text S3 in Supporting Information S1). We then examine the resulting suite of models. The individual entries in the ensemble of models are extremely similar visually (Figures S36 and S37 in Supporting Information S1), and variatiodns in the inverted structure are weak compared to the amplitude of variations that are interpreted. The mean of the ensemble has patterns that are extremely similar to our preferred model (Figure S38 in Supporting Information S1). This emphasizes that our choice of data weights do not control the interpreted features in the model.

Finally, we note that we also tested (Figure S39 in Supporting Information S1) the impact of controlling model roughness via first-derivative minimization (flatness) or second-derivative minimization (smoothness), the latter of which is used in the preferred model. We found that the differences between the two resultant δV_s models are minimal.

4. Discussion

4.1. Nature of Imaged Heterogeneity

Our first-order observation of substantial lateral velocity heterogeneity requires contrasts in state variables in the upper mantle beneath OldORCA. Seismic velocity is chiefly governed by temperature, composition, the presence of melt, and the activation of anelastic mechanisms (Abers et al., 2014; Dalton et al., 2009). Composition is an unlikely culprit for observed heterogeneity, since a 5% contrast would require ∼20% variation in SiO_2 content via melt depletion (Schutt & Lesher, 2006), which is implausible given normative contrasts in asthenospheric fertility (Morgan, 1997). We therefore consider to what extent temperature can explain observed structure, since the other factors are strong functions of this parameter. Accordingly, we compare δV_s to δV_p across the independent tomographic models. The ratio of these properties quantifies relative shear to bulk modulus variation, diagnostic of underlying physical mechanisms (D. L. Anderson, 2000;Goes et al., 2000). Figure S40 shows these corresponding values at co-located and well-resolved model nodes. The best-fitting $\delta V_s/\delta V_p$ slope of ∼1.38 is consistent with heterogeneity governed by thermal effects alone (1.2–2.0), and does not necessitate the presence of melt (O. L. Anderson et al., 1992; Eilon et al., 2015), though given the uncertainties in imaging, the presence of melt may still be consistent with the imaged structures.

Our models are perturbational in nature, and technically insensitive to absolute velocities. Thus, a central question is whether the slow and fast imaged anomalies correspond to mantle features that depart from ambient mantle (e.g., hotter and colder than the adiabat, respectively) or whether they merely differ relative to each other (Figure 9). The former scenario would require provision of heat, presumably from below, as well as cold-anomalies, presumably sourced from the base of the plate. The latter scenario would require cold (and absolutely fast) material descending from the plate into average mantle (normal velocity, apparently slower), or cells of hot (and absolutely slow) material ascending through average mantle (normal velocity, apparently faster). Average wavespeeds from surface wave imaging here (Russell et al., 2022) suggests that the overall upper mantle here is sitting roughly on an adiabatic temperature (for 1,350°C potential temperature). This suggests a purely "bottom-up" scenario is unlikely. We thus explore two possibilities: (a) Relatively slow features correspond to ambient mantle, and relatively fast features are cold. (b) Relatively slow features are on the adiabat but (perhaps due to volatiles) contain melt, relatively fast features are cold.

To address this, we quantify thermal anomalies compatible with the amplitudes of δV_s heterogeneity within the upper mantle, focusing on the depth range between 120 and 170 km. We fix the lowest velocities by using a

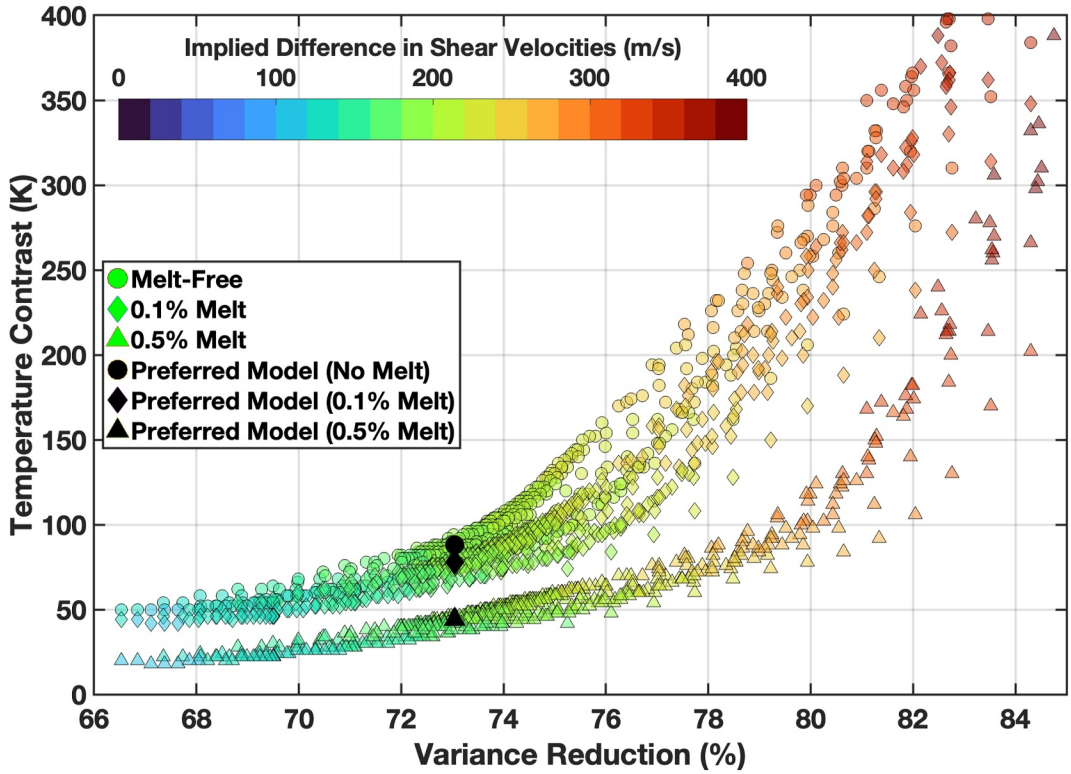

Figure 8. Thermal anomaly implied by the peak-to-peak velocity anomalies in our suite of shear-wave velocity models, spanning a wide range of damping and smoothing parameters. In this context, peak-to-peak velocity anomalies correspond to the difference between the 2.5th and the 97.5th percentile of the velocity anomalies. Circles correspond to a scenario with no melt, diamonds correspond to a scenario with a minimal amount of melt, and triangles correspond to a scenario with a modest amount of melt. Each plotted point corresponds to a different combination of smoothing and damping parameters.

temperature at 1350°C, corresponding to a potential temperature of 1,292 K assuming a 0.35 K/km adiabat. We implemented three scenarios with no melt fraction (A), a modest melt fraction of 0.5% (B), and a minimal melt fraction of 0.1% (Scenario C), which is similar geodynamically to (B). We then calculate a lookup table of V_s for (melt-free) mantle between 800 and 1350°C, to find the temperature contrast (relative to the slow endmember) required to match a given velocity contrast. We assume a lherzolite mantle composition, and calculate the corresponding anharmonic elastic moduli using the toolbox of Abers and Hacker (2016). We assume a grain size of 1 mm, a period of 10 s (consistent with the average frequency of *S*-wave measurements), and pressures corresponding to a depth of 145 km. Anelasticity is accounted for using the VBRc (Havlin et al., 2021), wherein we implement relaxation through the *xfit-premelt* scaling law of (Yamauchi & Takei, 2016), updated to include the direct effect of melt (Yamauchi & Takei, 2024). For the low-velocity endmember at 1350°C we obtain $V_s = 4.33$ km/s for case (A) with no melt, $V_s = 4.25$ km/s for case (B) with 0.5% melt fraction, and $V_s = 4.31$ km/s for case (C) with 0.1% melt fraction.

Since uncertainties associated with our choice of model regularization are likely larger than uncertainties in the V_s calculation, we explore the temperature anomalies associated with our full suite of regularization choices, using the setup described above. We convert from absolute to relative velocities by pinning the low end-member velocity to the 2.5th percentile deviatoric velocity in the tomographic model. We then use the VBRc lookup table above to calculate the temperature that would be required to get the corresponding (high) velocity at the 97.5th percentile δV_s. The difference between these temperatures yields the peak-to-peak thermal anomaly implied by a given tomographic model. We repeat this for all models in our L-test sweep of regularization parameters, so that the reader can decide for themselves what combination of data fit and implied thermal heterogeneity they find believable (Figure 8).

This analysis makes several things clear. As expected, the presence of melt trades off with temperature heterogeneity. At our preferred model (73% variance reduction), scenario (A) implies ~90 K thermal contrast between

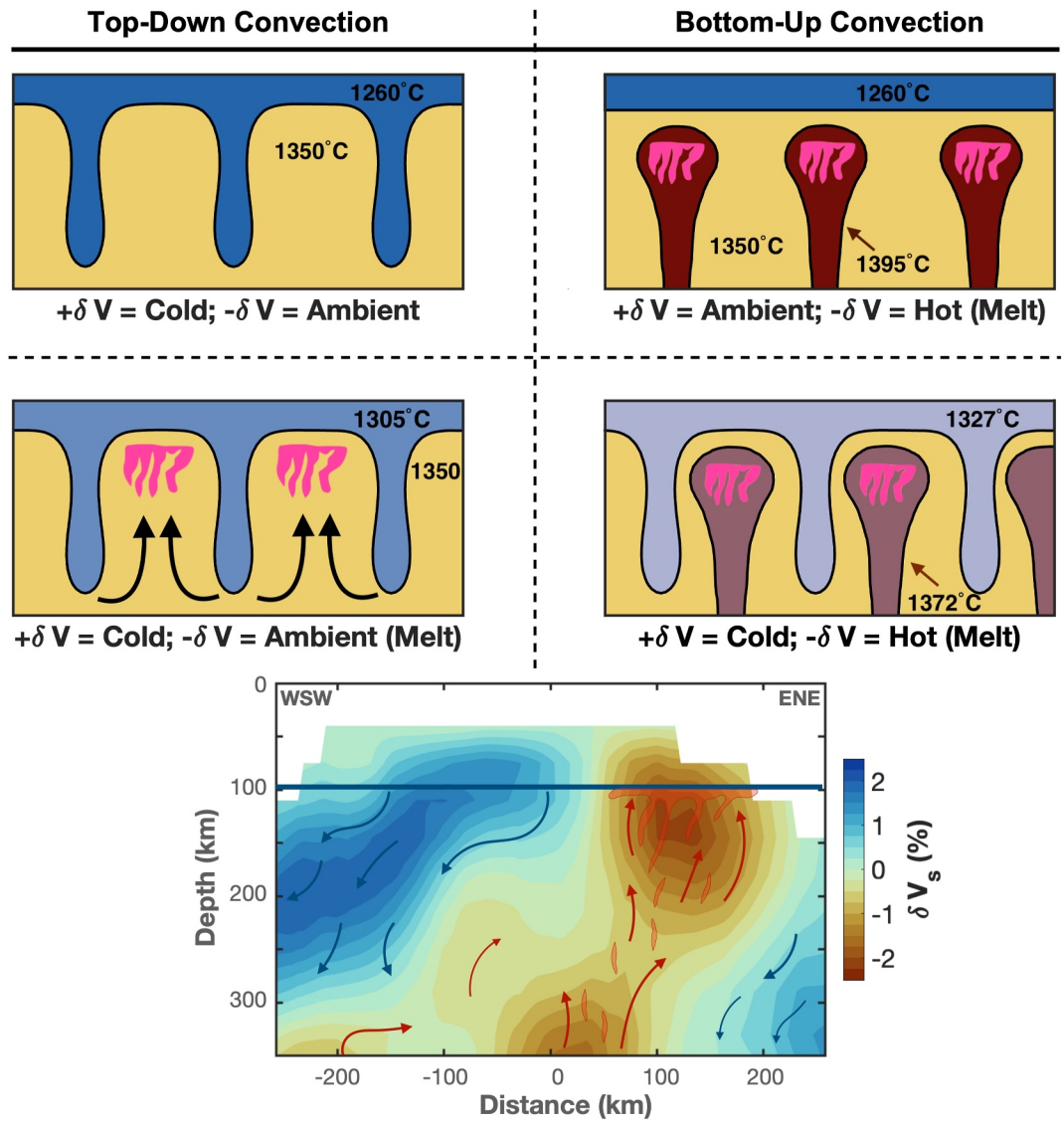

Figure 9. Schematic of possible scenarios for small-scale convective processes compatible with the peak-to-peak anomalies in our body-wave tomographic imaging. Each row either permits or does not allow melt, and each column represents a different set of driving forces for convective processes. In this schematic, the bottom-left panel is our preferred model. Temperatures resulting in our inferred temperature contrast of either ∼90 K (no melt) or ∼45 K (melt) are shown; the presence of melt is indicated by orange lenses. The bottom panel shows an annotated cross-section of our preferred *S*-wave tomographic model, with arrows indicating convective dynamics; the solid line corresponds to the depth to the 1,150 isotherm for 90 Ma seafloor.

fast/slow regions, while scenario (B) requires only 45 K, along with 0.5% melt in the slow structures. A higher data fit is possible but would require a larger temperature contrast, on the order of ≥200 K for 78% variance reduction for scenario A. Scenario (C) is a compromise between these two scenarios, showing that a subtle (0.1%) amount of melt can reduce the implied thermal anomaly by a small amount, on the order of 10 K, implying an 80 K thermal contrast. Unless substantial melt is present, even poorly fit, over-damped models require non-zero thermal heterogeneity. Attributing structure to mostly temperature variation, potentially with a minimal amount of melt, is consistent with the scaling between the *P* and *S* models. A note of caution is that body-wave tomographic images generally under-predict the amplitude of velocity heterogeneity (Burdick & Lekić, 2017); therefore, the above inferred thermal anomalies might be lower bounds. Below, we discuss our preferred scenario.

4.2. Implications for Dynamic Processes

Our preferred model shows mantle heterogeneity at uppermost mantle depths ($z \approx 80$ km; Figure 3). This heterogeneity may reflect convective instabilities driven from the "top-down" by gravitationally unstable lithosphere; the relatively high-velocity anomalies being the active downwelling lithosphere (Conrad & Molnar, 1999) and slow anomalies being upwelling asthenosphere that is displaced by the downwellings. It is reasonable for slow regions to contain some melt as adiabatic upwellings cross the solidus during ascent. An alternate hypothesis is that convective cells are driven from the "bottom-up", whereby deeper-sourced hot mini-plumes deform or destabilize the base of the lithosphere. Such upwellings could be linked to abundant south Pacific hotspot activity (Davaille & Romanowicz, 2020; Yamamoto et al., 2007) and/or the Pacific LLSVP (Lekic et al., 2012; Munch et al., 2024). This latter scenario, with hot material ascending from depth, would predict reduced thickness of the mantle transition zone beneath the region.

We favor the "top-down" model for the active convective processes that we image. The large age of the study region provides sufficient time for gravitational instabilities to form at the base of the plates. 'Rolls' induced by sub-lithospheric small-scale convection (SSC) should align with the orientation of plate motion (van Hunen & Zhong, 2006), as convective cells are sheared by an overriding plate (Haxby & Weissel, 1986). This is roughly what we see - our best-fitting model lineation (325° for *P*, 340° for *S*) is subparallel to absolute plate motion (301.44° in a NNR reference frame). The orientation of the lithospheric heterogeneity in our model is slightly closer to the orientation of the free-air gravity anomalies, which may suggest a link between imaged lithospheric structure and shallower processes. The amplitude of the inferred thermal anomaly provides an additional metric to validate different models for the convective processes implied by our tomography. Dannberg et al. (2025) show, using fully 3D geodynamic simulations of small-scale convection, that the temperature anomalies associated with cold lithospheric downwellings are typically −75 K or less, broadly consistent with our results. Moreover, since positive thermal anomalies of substantial magnitude are unlikely to be sourced within the asthenosphere or at its base, the corresponding bottom-up scenario for convective heterogeneity likely necessitates thermal anomalies introduced by a plume or mantle upwelling. Such temperature anomalies associated with mantle upwellings are larger, often in excess of 200 K (Putirka, 2005; Sleep, 1990). Thus, the temperature anomalies associated with our preferred tomographic model (50–100 K, depending on the presence of melt) are more consistent with a scenario of small-scale convection due to lithospheric downwelling.

However, geophysical observations at the surface do not obviously support a link to the tomographically imaged mantle structure. The OldORCA region contains a number of small, semi-parallel volcanic ridges or seamount chains that are flanked by FAA lows, suggesting flexural compensation (Figure 1). Judging from the width of the FAA lows, the characteristic flexural wavelength appears to be on the order of 25 km, although some spatial variation is evident. A flexural wavelength of 25 km translates to an effective elastic thickness of only a few km, comparable to the thickness found in much of the GLIMPSE study area (Harmon et al., 2006). Thus, much of the bathymetric and FAA variation in old ORCA could be due to frozen-in features formed when the seafloor was very young, and may not necessarily be expected to reflect heterogeneity in our tomographic images. Some, though not all, seamounts here have angular, stellate morphology corresponding to radial dyke zones. This suggests they have experienced mass wasting following slow alteration by seawater, likely indicative of old edifices (Mitchell, 2001; Vogt & Smoot, 1984). Moreover, the locations of the seamounts do not agree well with the locations of low-velocity tomographic anomalies (Figure 2), as one might expect if they were due to recent melt production in an SSC system (Ballmer et al., 2007). Thus, either these seamounts reflect a long-extinct process totally independent of contemporary SSC, or some complex plumbing system allows volcanism to be offset laterally from the shallow low-velocity model anomalies that we presume to be upwellings.

Dynamical simulations (Ballmer et al., 2007; Dannberg et al., 2024) have highlighted the possibility of SSC at a wide range of locations and lithospheric ages. This may be a common process throughout the oceanic upper mantle. A growing suite of OBS body-wave tomography studies are consistent with SSC in oceanic asthenosphere. Kang et al. (2023) and Eilon, Zhang, et al. (2022) image substantial velocity heterogeneity, and differential arrival times measured at the NoMelt array show substantial amplitude (Hung et al., 2017), consistent with sharp velocity heterogeneity. In fact, to date, no body-wave imaging studies beneath stable oceanic lithosphere have imaged weak or absent heterogeneity (Eilon, Zhang, et al., 2022; Hung et al., 2017; Kang et al., 2023). The imaging results shown here, validated by independent sets of measurements for *P* and *S* waves, provide additional support for widespread SSC.

The dynamical implications of this process being common are profound. SSC may explain observed shallowing in age-depth profiles (Crosby et al., 2006; Stein & Stein, 1992), and control the thickness of the oceanic lithosphere (Priestley & McKenzie, 2006; Ritzwoller et al., 2004). Furthermore, the partial melt owing to SSC may pond, or have frozen, in laterally variable amounts at the plates' base (Rychert et al., 2020), explaining widespread observations of a sharp discontinuity in the oceanic lithosphere-asthenosphere system (Chen et al., 2024; Mark et al., 2021; Schmerr, 2012; Tharimena et al., 2017). SSC could also contribute to sharp lithospheric discontinuities through other mechanisms. For instance, to satisfy strain continuity across a shallow viscosity boundary (Hirth & Kohlstedt, 1996), the deformation associated with SSC may result in a seismically detectable change in grain size. In addition, if SSC introduces new volatiles from depth, this could locally depress the solidus, reducing shear velocities through a pre-melt effect (Yamauchi & Takei, 2020).

Given the pervasive nature of small-scale heterogeneity suggested by observations, it may be auspicious to refine paradigms of a homogeneous oceanic upper mantle and consider more rigorously the implications of fairly ubiquitious convective processes, especially where gravity lineations are present.

5. Conclusion

We present tomographic images of the oceanic upper mantle beneath old oceanic lithosphere, using new *P* and *S*-wave traveltime measurements. Our velocity models contain strong heterogeneity that implies substantial ($\lesssim$100 K) thermal variations in the sublithospheric mantle and/or more subtle thermal variations ($\sim$50 K) alongside regions with partial melt. The imaged heterogeneity is moderately lineated (particularly at shallower depths), with elongation subparallel to both free-air gravity lineations and the orientation of absolute plate motion. This supports an interpretation that the velocity anomalies represent small-scale convection driven by boundary layer instabilities at the base of the plate. The number of broadband OBS studies that document observational evidence of sub-lithospheric small-scale convection continues to grow, lending support to a scenario where convective processes are common throughout the oceanic upper mantle.

Conflict of Interest

The authors declare no conflicts of interest relevant to this study.

Data Availability Statement

Broadband seismic data used in this study can be downloaded from the SAGE data management center under the network code **7B**. The OldORCA segment of the PacificORCA deployment is attributable to the DOI https://doi.org/10.7914/SN/7B_2019 (Gaherty et al., 2019), and the YoungORCA segment of the PacificORCA deployment is attributable to the DOI https://doi.org/10.7914/1yaj-fm53 (Gaherty et al., 2018). Plate motion calculations were conducted using the GAGE plate motion calculator at https://www.unavco.org/software/geodetic-utilities/plate-motion-calculator/plate-motion-calculator.html. Software to make the body-wave traveltime measurements is archived on Zenodo (Eilon, 2025). The 3-D velocity models generated in this study are provided in the supporting information (Data Set S1). Data were accessed from the NSF SAGE data archive operated by EarthScope Consortium (NSF award 1724509).

Acknowledgments
This research was supported by the National Science Foundation through NSF Grants OCE-1658214, OCE-2051265, OCE-1658070, and OCE-2143865. Some figures were made using the colormaps from Crameri et al. (2020). Some figures were made using the M_Map toolbox (Pawlowicz, 2020) and with GMT6 (Wessel et al., 2019). We gratefully acknowledge the support from SIO with managing their fleet of OBS instruments, and well as the crew and operators of the *Kilo Moana* and *Roger Revelle* vessels that made the OBS deployment and recovery cruises involved in securing the data in this study possible. We acknowledge useful discussions with Cristhian Salas, Brennan Brunsvik, and Keneni Godana. We thank the associate editor and Guust Nolet for useful reviews that have improved the manuscript.

References

Abers, G. A., Fischer, K., Hirth, G., Wiens, D., Plank, T., Holtzman, B. K., et al. (2014). Reconciling mantle attenuation-temperature relationships from seismology, petrology, and laboratory measurements. *Geochemistry, Geophysics, Geosystems*, *15*(9), 3521–3542. https://doi.org/10.1002/2014gc005444

Abers, G. A., & Hacker, B. R. (2016). A matlab toolbox and e xcel workbook for calculating the densities, seismic wave speeds, and major element composition of minerals and rocks at pressure and temperature. *Geochemistry, Geophysics, Geosystems*, *17*(2), 616–624. https://doi.org/10.1002/2015gc006171

Affonso, G., Rocha, M., Costa, I., Assumpção, M., Fuck, R., Albuquerque, D., et al. (2021). Lithospheric architecture of the paranapanema block and adjacent nuclei using multiple-frequency p-wave seismic tomography. *Journal of Geophysical Research: Solid Earth*, *126*(4), e2020JB021183. https://doi.org/10.1029/2020jb021183

Altamimi, Z., Rebischung, P., Collilieux, X., Métivier, L., & Chanard, K. (2023). Itrf2020: An augmented reference frame refining the modeling of nonlinear station motions. *Journal of Geodesy*, *97*(5), 47. https://doi.org/10.1007/s00190-023-01738-w

Anderson, D. L. (2000). The thermal state of the upper mantle; no role for mantle plumes. *Geophysical Research Letters*, *27*(22), 3623–3626. https://doi.org/10.1029/2000gl011533

Anderson, O. L., Isaak, D., & Oda, H. (1992). High-temperature elastic constant data on minerals relevant to geophysics. *Reviews of Geophysics*, *30*(1), 57–90. https://doi.org/10.1029/91rg02810

Ballmer, M., Van Hunen, J., Ito, G., Tackley, P., & Bianco, T. (2007). Non-hotspot volcano chains originating from small-scale sublithospheric convection. *Geophysical Research Letters*, *34*(23). https://doi.org/10.1029/2007gl031636

Brunsvik, B. R., Eilon, Z. C., & Lynner, C. (2021). Mantle structure and flow across the continent-ocean transition of the eastern North American margin: Anisotropic s-wave tomography. *Geochemistry, Geophysics, Geosystems*, *22*(12), e2021GC010084. https://doi.org/10.1029/2021gc010084

Buck, W. R., & Parmentier, E. (1986). Convection beneath young oceanic lithosphere: Implications for thermal structure and gravity. *Journal of Geophysical Research*, *91*(B2), 1961–1974. https://doi.org/10.1029/jb091ib02p01961

Burdick, S., & Lekić, V. (2017). Velocity variations and uncertainty from transdimensional p-wave tomography of North America. *Geophysical Journal International*, *209*(2), 1337–1351. https://doi.org/10.1093/gji/ggx091

Cazenave, A., Houry, S., Lago, B., & Dominh, K. (1992). Geosat-derived geoid anomalies at medium wavelength. *Journal of Geophysical Research*, *97*(B5), 7081–7096. https://doi.org/10.1029/91jb03127

Chen, K.-X., Forsyth, D., & Fischer, K. (2024). A mid-lithospheric discontinuity detected beneath 155 Ma western pacific seafloor using sp receiver functions. *Geophysical Research Letters*, *51*(5), e2024GL108347. https://doi.org/10.1029/2024gl108347

Cochran, J. R. (1986). Variations in subsidence rates along intermediate and fast spreading mid-ocean ridges. *Geophysical Journal International*, *87*(2), 421–454. https://doi.org/10.1111/j.1365-246x.1986.tb06631.x

Conder, J. A., Forsyth, D. W., & Parmentier, E. (2002). Asthenospheric flow and asymmetry of the east pacific rise, melt area. *Journal of Geophysical Research*, *107*(B12), ETG-8. https://doi.org/10.1029/2001jb000807

Conrad, C., & Molnar, P. (1999). Convective instability of a boundary layer with temperature-and strain-rate-dependent viscosity in terms of 'available buoyancy. *Geophysical Journal International*, *139*(1), 51–68. https://doi.org/10.1046/j.1365-246x.1999.00896.x

Crameri, F., Shephard, G. E., & Heron, P. J. (2020). The misuse of colour in science communication. *Nature Communications*, *11*(1), 5444. https://doi.org/10.1038/s41467-020-19160-7

Crosby, A., McKenzie, D., & Sclater, J. (2006). The relationship between depth, age and gravity in the oceans. *Geophysical Journal International*, *166*(2), 553–573. https://doi.org/10.1111/j.1365-246x.2006.03015.x

Crough, S. T. (1978). Thermal origin of mid-plate hot-spot swells. *Geophysical Journal International*, *55*(2), 451–469. https://doi.org/10.1111/j.1365-246x.1978.tb04282.x

Dalton, C. A., Ekström, G., & Dziewonski, A. M. (2009). Global seismological shear velocity and attenuation: A comparison with experimental observations. *Earth and Planetary Science Letters*, *284*(1–2), 65–75. https://doi.org/10.1016/j.epsl.2009.04.009

Dannberg, J., Eilon, Z., Russell, J. B., & Gassmoeller, R. (2024). Sub-lithospheric small-scale convection as a window into the asthenosphere: Insights from integrating models of mantle convection, grain size evolution and seismic tomography (technical report). *Copernicus Meetings*.

Dannberg, J., Eilon, Z., Russell, J. B., & Gassmöller, R. (2025). Understanding sub-lithospheric small-scale convection by linking models of grain size evolution, mantle convection, and seismic tomography. *Geochemistry, Geophysics, Geosystems*, *26*(9), e2025GC012289. https://doi.org/10.1029/2025GC012289

Davaille, A., & Romanowicz, B. (2020). Deflating the LLSVPs: Bundles of mantle thermochemical plumes rather than thick stagnant "piles". *Tectonics*, *39*(10), e2020TC006265. https://doi.org/10.1029/2020tc006265

Eagles, G., Gohl, K., & Larter, R. D. (2004). High-resolution animated tectonic reconstruction of the South Pacific and West Antarctic Margin. *Geochemistry, Geophysics, Geosystems*, *5*(7), Q07002. https://doi.org/10.1029/2003gc000657

Eilon, Z. (2025). Attenbody: Release v1.0.0 [Software]. *Zenodo*. https://doi.org/10.5281/zenodo.17510396

Eilon, Z., Abers, G. A., Gaherty, J. B., & Jin, G. (2015). Imaging continental breakup using teleseismic body waves: The woodlark rift, Papua New Guinea. *Geochemistry, Geophysics, Geosystems*, *16*(8), 2529–2548. https://doi.org/10.1002/2015GC005835

Eilon, Z., Gaherty, J. B., Zhang, L., Russell, J., McPeak, S., Phillips, J., et al. (2022). The pacific OBS research into convecting asthenosphere (orca) experiment. *Seismological Society of America*, *93*(1), 477–493. https://doi.org/10.1785/0220210173

Eilon, Z., Zhang, L., Gaherty, J. B., Forsyth, D. W., & Russell, J. B. (2022). Sub-lithospheric small-scale convection tomographically imaged beneath the pacific plate. *Geophysical Research Letters*, *49*(18), e2022GL100351. https://doi.org/10.1029/2022GL100351

Forsyth, D. W. (1992). Geophysical constraints on mantle flow and melt generation beneath mid-ocean ridges. *Geophysical Monograph Series*, *71*, 1–65. https://doi.org/10.1029/gm071p0001

Forsyth, D. W., Harmon, N., Scheirer, D. S., & Duncan, R. A. (2006). Distribution of recent volcanism and the morphology of seamounts and ridges in the glimpse study area: Implications for the lithospheric cracking hypothesis for the origin of intraplate, non–hot spot volcanic chains. *Journal of Geophysical Research*, *111*(B11), e2022GL100351. https://doi.org/10.1029/2005jb004075

Gaherty, J., Eilon, Z., Forsyth, D., & Ekstrom, G. (2018). Pacific Array—Young ORCA [Dataset]. *International Federation of Digital Seismograph Networks*. https://doi.org/10.7914/1yaj-fm53

Gaherty, J., Eilon, Z., Forsyth, D., & Ekström, G. (2019). PacificORCA [Dataset]. *International Federation of Digital Seismograph Networks*. https://doi.org/10.7914/SN/7B_2019

Gee, J. S., Cande, S. C., Kent, D. V., Partner, R., & Heckman, K. (2008). Mapping geomagnetic field variations with unmanned airborne vehicles. *Eos, Transactions American Geophysical Union*, *89*(19), 178–179. https://doi.org/10.1029/2008eo190002

Goes, S., Govers, R., & Vacher, P. (2000). Shallow mantle temperatures under Europe from P and S wave tomography. *Journal of Geophysical Research*, *105*(B5), 11153–11169. https://doi.org/10.1029/1999jb900300

Harmon, N., Forsyth, D. W., Lamm, R., & Webb, S. C. (2007). P and S wave delays beneath intraplate volcanic ridges and gravity lineations near the east pacific rise. *Journal of Geophysical Research*, *112*(B3), B03309. https://doi.org/10.1029/2006jb004392

Harmon, N., Forsyth, D. W., & Scheirer, D. S. (2006). Analysis of gravity and topography in the glimpse study region: Isostatic compensation and uplift of the sojourn and hotu matua ridge systems. *Journal of Geophysical Research*, *111*(B11), B11406. https://doi.org/10.1029/2005jb004071

Harmon, N., Forsyth, D. W., Weeraratne, D. S., Yang, Y., & Webb, S. C. (2011). Mantle heterogeneity and off axis volcanism on young pacific lithosphere. *Earth and Planetary Science Letters*, *311*(3–4), 306–315. https://doi.org/10.1016/j.epsl.2011.09.038

Havlin, C., Holtzman, B. K., & Hopper, E. (2021). Inference of thermodynamic state in the asthenosphere from anelastic properties, with applications to North American upper mantle. *Physics of the Earth and Planetary Interiors*, *314*, 106639. https://doi.org/10.1016/j.pepi.2020.106639

Haxby, W. F., & Weissel, J. K. (1986). Evidence for small-scale mantle convection from Seasat altimeter data. *Journal of Geophysical Research*, *91*(B3), 3507–3520. https://doi.org/10.1029/jb091ib03p03507

Hirth, G., & Kohlstedt, D. L. (1996). Water in the oceanic upper mantle: Implications for rheology, melt extraction and the evolution of the lithosphere. *Earth and Planetary Science Letters*, *144*(1–2), 93–108. https://doi.org/10.1016/0012-821x(96)00154-9

Holmes, R. C., Webb, S. C., & Forsyth, D. W. (2007). Crustal structure beneath the gravity lineations in the gravity lineations, intraplate melting, petrologic and seismic expedition (glimpse) study area from seismic refraction data. *Journal of Geophysical Research*, *112*(B7). https://doi.org/10.1029/2006jb004685

Hung, S.-H., Shen, Y., & Chiao, L.-Y. (2004). Imaging seismic velocity structure beneath the Iceland hot spot: A finite frequency approach. *Journal of Geophysical Research*, *109*(B8), B08305. https://doi.org/10.1029/2003jb002889

Hung, S.-H., Dahlen, F., & Nolet, G. (2000). Fréchet kernels for finite-frequency traveltimeséii. Examples. *Geophysical Journal International*, *141*(1), 175–203. https://doi.org/10.1046/j.1365-246x.2000.00072.x

Hung, S.-H., Lin, P.-Y., Gaherty, J. B., Russell, J. B., Jin, G., Collins, J. A., et al. (2017). Seismic velocity structure of the Pacific upper mantle in the nomelt region from finite-frequency traveltime tomography. In *Agu fall meeting abstracts* (Vol. 2017, p. S32C-02).

Janiszewski, H. A., Eilon, Z., Russell, J., Brunsvik, B., Gaherty, J., Mosher, S., et al. (2023). Broad-band ocean bottom seismometer noise properties. *Geophysical Journal International*, *233*(1), 297–315. https://doi.org/10.1093/gji/ggac450

Kang, H., Kim, Y., Hung, S.-H., Lin, P.-Y. P., Isse, T., Kawakatsu, H., et al. (2023). Seismic velocity structure of upper mantle beneath the oldest Pacific seafloor: Insights from finite-frequency tomography. *Geochemistry, Geophysics, Geosystems*, *24*(9), e2022GC010833. https://doi.org/10.1029/2022gc010833

Karato, S.-I. (1993). Importance of anelasticity in the interpretation of seismic tomography. *Geophysical Research Letters*, *20*(15), 1623–1626. https://doi.org/10.1029/93gl01767

Kennett, B., & Engdahl, E. (1991). Traveltimes for global earthquake location and phase identification. *Geophysical Journal International*, *105*(2), 429–465. https://doi.org/10.1111/j.1365-246x.1991.tb06724.x

Kim, S.-S., & Wessel, P. (2011). New global seamount census from altimetry-derived gravity data. *Geophysical Journal International*, *186*(2), 615–631. https://doi.org/10.1111/j.1365-246x.2011.05076.x

Korenaga, T., & Korenaga, J. (2008). Subsidence of normal oceanic lithosphere, apparent thermal expansivity, and seafloor flattening. *Earth and Planetary Science Letters*, *268*(1–2), 41–51. https://doi.org/10.1016/j.epsl.2007.12.022

Lekic, V., Cottaar, S., Dziewonski, A., & Romanowicz, B. (2012). Cluster analysis of global lower mantle tomography: A new class of structure and implications for chemical heterogeneity. *Earth and Planetary Science Letters*, *357*, 68–77. https://doi.org/10.1016/j.epsl.2012.09.014

Mark, H., Collins, J., Lizarralde, D., Hirth, G., Gaherty, J., Evans, R., & Behn, M. (2021). Constraints on the depth, thickness, and strength of the g discontinuity in the central Pacific from s receiver functions. *Journal of Geophysical Research: Solid Earth*, *126*(4), e2019JB019256. https://doi.org/10.1029/2019jb019256

Marquering, H., Dahlen, F., & Nolet, G. (1999). Three-dimensional sensitivity kernels for finite-frequency traveltimes: The banana-doughnut paradox. *Geophysical Journal International*, *137*(3), 805–815. https://doi.org/10.1046/j.1365-246x.1999.00837.x

Mitchell, N. C. (2001). Transition from circular to stellate forms of submarine volcanoes. *Journal of Geophysical Research*, *106*(B2), 1987–2003. https://doi.org/10.1029/2000jb900263

Montelli, R., Nolet, G., Masters, G., Dahlen, F., & Hung, S.-H. (2004). Global p and pp traveltime tomography: Rays versus waves. *Geophysical Journal International*, *158*(2), 637–654. https://doi.org/10.1111/j.1365-246x.2004.02346.x

Morgan, J. P. (1997). The generation of a compositional lithosphere by mid-ocean ridge melting and its effect on subsequent off-axis hotspot upwelling and melting. *Earth and Planetary Science Letters*, *146*(1–2), 213–232. https://doi.org/10.1016/s0012-821x(96)00207-5

Munch, F. D., Romanowicz, B., Mukhopadhyay, S., & Rudolph, M. L. (2024). Deep mantle plumes feeding periodic alignments of asthenospheric fingers beneath the central and southern Atlantic Ocean. *Proceedings of the National Academy of Sciences*, *121*(46), e2407543121. https://doi.org/10.1073/pnas.2407543121

Paige, C. C., & Saunders, M. A. (1982). Lsqr: An algorithm for sparse linear equations and sparse least squares. *ACM Transactions on Mathematical Software*, *8*(1), 43–71. https://doi.org/10.1145/355984.355989

Parker, R., & Oldenburg, D. (1973). Thermal model of ocean ridges. *Nature; Physical Science*, *242*(122), 137–139. https://doi.org/10.1038/physci242137a0

Parsons, B., & Daly, S. (1983). The relationship between surface topography, gravity anomalies, and temperature structure of convection. *Journal of Geophysical Research*, *88*(B2), 1129–1144. https://doi.org/10.1029/jb088ib02p01129

Parsons, B., & McKenzie, D. (1978). Mantle convection and the thermal structure of the plates. *Journal of Geophysical Research*, *83*(B9), 4485–4496. https://doi.org/10.1029/jb083ib09p04485

Parsons, B., & Sclater, J. G. (1977). An analysis of the variation of ocean floor bathymetry and heat flow with age. *Journal of Geophysical Research*, *82*(5), 803–827. https://doi.org/10.1029/jb082i005p00803

Pawlowicz, R. (2020). M_map: A mapping package for Matlab. *Computer Software*.

Phillips, J., Gaherty, J. B., Russell, J. B., Eilon, Z., Forsyth, D. W., & Byrnes, J. S. (2023). Spatial variation in anisotropic shear velocity of old Oceanic lithosphere-asthenosphere in the Southwest Pacific. In *Agu fall meeting abstracts, 2023, DI42A-01*.

Priestley, K., & McKenzie, D. (2006). The thermal structure of the lithosphere from shear wave velocities. *Earth and Planetary Science Letters*, *244*(1–2), 285–301. https://doi.org/10.1016/j.epsl.2006.01.008

Putirka, K. D. (2005). Mantle potential temperatures at Hawaii, Iceland, and the mid-ocean ridge system, as inferred from olivine phenocrysts: Evidence for thermally driven mantle plumes. *Geochemistry, Geophysics, Geosystems*, *6*(5). https://doi.org/10.1029/2005GC000915

Richards, M. A., & Hager, B. H. (1989). Effects of lateral viscosity variations on long-wavelength geoid anomalies and topography. *Journal of Geophysical Research*, *94*(B8), 10299–10313. https://doi.org/10.1029/jb094ib08p10299

Richter, F. M., & Parsons, B. (1975). On the interaction of two scales of convection in the mantle. *Journal of Geophysical Research*, *80*(17), 2529–2541. https://doi.org/10.1029/jb080i017p02529

Ritsema, J., & Lekić, V. (2020). Heterogeneity of seismic wave velocity in earth's mantle. *Annual Review of Earth and Planetary Sciences*, *48*(1), 377–401. https://doi.org/10.1146/annurev-earth-082119-065909

Ritzwoller, M., Masters, G., & Gilbert, F. (1988). Constraining aspherical structure with low-degree interaction coefficients: Application to uncoupled multiplets. *Journal of Geophysical Research*, *93*(B6), 6369–6396. https://doi.org/10.1029/jb093ib06p06369

Ritzwoller, M., Shapiro, N., & Zhong, S.-J. (2004). Cooling history of the pacific lithosphere. *Earth and Planetary Science Letters*, *226*(1–2), 69–84. https://doi.org/10.1016/j.epsl.2004.07.032

Russell, J. B., Dalton, C. A., Havlin, C., & Holtzman, B. K. (2022). Quantifying asthenospheric temperature and partial melt in the Pacific using ocean-bottom observations of shear attenuation and velocity. In *Agu fall meeting abstracts, 2022* (p. DI25C-0038).

Rychert, C. A., Harmon, N., Constable, S., & Wang, S. (2020). The nature of the lithosphere-asthenosphere boundary. *Journal of Geophysical Research: Solid Earth*, *125*(10), e2018JB016463. https://doi.org/10.1029/2018jb016463

Sandwell, D. T., & Fialko, Y. (2004). Warping and cracking of the Pacific plate by thermal contraction. *Journal of Geophysical Research*, *109*(B10). https://doi.org/10.1029/2004jb003091

Sandwell, D. T., Müller, R. D., Smith, W. H., Garcia, E., & Francis, R. (2014). New global marine gravity model from Cryosat-2 and Jason-1 reveals buried tectonic structure. *Science*, *346*(6205), 65–67. https://doi.org/10.1126/science.1258213

Sandwell, D. T., Winterer, E. L., Mammerickx, J., Duncan, R. A., Lynch, M. A., Levitt, D. A., & Johnson, C. L. (1995). Evidence for diffuse extension of the Pacific plate from pukapuka ridges and cross-grain gravity lineations. *Journal of Geophysical Research*, *100*(B8), 15087–15099. https://doi.org/10.1029/95jb00156

Schmandt, B., & Humphreys, E. (2010). Seismic heterogeneity and small-scale convection in the southern California upper mantle. *Geochemistry, Geophysics, Geosystems*, *11*(5), Q05004. https://doi.org/10.1029/2010gc003042

Schmerr, N. (2012). The gutenberg discontinuity: Melt at the lithosphere-asthenosphere boundary. *Science*, *335*(6075), 1480–1483. https://doi.org/10.1126/science.1215433

Schutt, D., & Lesher, C. (2006). Effects of melt depletion on the density and seismic velocity of garnet and spinel lherzolite. *Journal of Geophysical Research*, *111*(B5). https://doi.org/10.1029/2003jb002950

Sclater, J. G., & Francheteau, J. (1970). The implications of terrestrial heat flow observations on current tectonic and geochemical models of the crust and upper mantle of the earth. *Geophysical Journal International*, *20*(5), 509–542. https://doi.org/10.1111/j.1365-246x.1970.tb06089.x

Seton, M., Müller, R. D., Zahirovic, S., Williams, S., Wright, N. M., Cannon, J., et al. (2020). A global data set of present-day oceanic crustal age and seafloor spreading parameters. *Geochemistry, Geophysics, Geosystems*, *21*(10), e2020GC009214. https://doi.org/10.1029/2020gc009214

Sleep, N. H. (1969). Sensitivity of heat flow and gravity to the mechanism of sea-floor spreading. *Journal of Geophysical Research*, *74*(2), 542–549. https://doi.org/10.1029/jb074i002p00542

Sleep, N. H. (1990). Hotspots and mantle plumes: Some phenomenology. *Journal of Geophysical Research*, *95*(B5), 6715–6736. https://doi.org/10.1029/JB095iB05p06715

Stein, C. A., & Stein, S. (1992). A model for the global variation in oceanic depth and heat flow with lithospheric age. *Nature*, *359*(6391), 123–129. https://doi.org/10.1038/359123a0

Tharimena, S., Rychert, C., Harmon, N., & White, P. (2017). Imaging pacific lithosphere seismic discontinuities—Insights from SS precursor modeling. *Journal of Geophysical Research: Solid Earth*, *122*(3), 2131–2152. https://doi.org/10.1002/2016jb013526

Toomey, D., Wilcock, W., Conder, J., Forsyth, D., Blundy, J., Parmentier, E., & Hammond, W. (2002). Asymmetric mantle dynamics in the melt region of the east Pacific rise. *Earth and Planetary Science Letters*, *200*(3–4), 287–295. https://doi.org/10.1016/s0012-821x(02)00655-6

Tozer, B., Sandwell, D. T., Smith, W. H., Olson, C., Beale, J. R., & Wessel, P. (2019). Global bathymetry and topography at 15 arc sec: SRTM15+. *Earth and Space Science*, *6*(10), 1847–1864. https://doi.org/10.1029/2019ea000658

Van Avendonk, H. J., Davis, J. K., Harding, J. L., & Lawver, L. A. (2017). Decrease in oceanic crustal thickness since the breakup of Pangaea. *Nature Geoscience*, *10*(1), 58–61. https://doi.org/10.1038/ngeo2849

VanDecar, J., & Crosson, R. (1990). Determination of teleseismic relative phase arrival times using multi-channel cross-correlation and least squares. *Bulletin of the Seismological Society of America*, *80*(1), 150–169.

van Hunen, J., & Zhong, S. (2006). Influence of rheology on realignment of mantle convective structure with plate motion after a plate reorganization. *Geochemistry, Geophysics, Geosystems*, *7*(8). https://doi.org/10.1029/2005gc001209

Vogt, P. R., & Smoot, N. C. (1984). The geisha guyots: Multibeam bathymetry and morphometric interpretation. *Journal of Geophysical Research*, *89*(B13), 11085–11107. https://doi.org/10.1029/jb089ib13p11085

Weeraratne, D. S., Forsyth, D. W., Yang, Y., & Webb, S. C. (2007). Rayleigh wave tomography beneath intraplate volcanic ridges in the south Pacific. *Journal of Geophysical Research*, *112*(B6). https://doi.org/10.1029/2006jb004403

Wessel, P., Luis, J. F., Uieda, L., Scharroo, R., Wobbe, F., Smith, W. H. F., & Tian, D. (2019). The generic mapping tools version 6. *Geochemistry, Geophysics, Geosystems*, *20*(11), 5556–5564. https://doi.org/10.1029/2019GC008515

Yamamoto, M., Morgan, J. P., & Morgan, W. J. (2007). Global plume-fed asthenosphere flow—I: Motivation and model development. *Special Paper 430: Plates, Plumes and Planetary Processes*, 165–188. https://doi.org/10.1130/2007.2430(09)

Yamauchi, H., & Takei, Y. (2016). Polycrystal anelasticity at near-solidus temperatures. *Journal of Geophysical Research: Solid Earth*, *121*(11), 7790–7820. https://doi.org/10.1002/2016jb013316

Yamauchi, H., & Takei, Y. (2020). Application of a premelting model to the lithosphere-asthenosphere boundary. *Geochemistry, Geophysics, Geosystems*, *21*(11), e2020GC009338. https://doi.org/10.1029/2020gc009338

Yamauchi, H., & Takei, Y. (2024). Effect of melt on polycrystal anelasticity. *Journal of Geophysical Research: Solid Earth*, *129*(4), e2023JB027738. https://doi.org/10.1029/2023jb027738

References From the Supporting Information

Amante, C., & Eakins, B. W. (2009). Etopo1 arc-minute global relief model: Procedures, data sources and analysis.